Influence of yield surface curvature on the macroscopic yielding and ductile failure of isotropic porous plastic materials

Lars Edvard Bryhni Dæhli*, David Morin, Tore Børvik, Odd Sture Hopperstad

Structural Impact Laboratory (SIMLab), Department of Structural Engineering, Norwegian University of Science and Technology (NTNU), NO-7491 Trondheim, Norway

Abstract

Numerical unit cell models of an approximative representative volume element for a porous ductile solid are utilized to investigate differences in the mechanical response between a quadratic and a non-quadratic matrix yield surface. A Hershey equivalent stress measure with two distinct values of the yield surface exponent is employed as the matrix description. Results from the unit cell calculations are further used to calibrate a heuristic extension of the Gurson model which incorporates effects of the third deviatoric stress invariant. An assessment of the porous plasticity model reveals its ability to describe the unit cell response to some extent, however underestimating the effect of the Lode parameter for the lower triaxiality ratios imposed in this study when compared to unit cell simulations. Ductile failure predictions by means of finite element simulations using a unit cell model that resembles an imperfection band are then conducted to examine how the non-quadratic matrix yield surface influences the failure strain as compared to the quadratic matrix yield surface. Further, strain localization predictions based on bifurcation analyses and imperfection band analyses are undertaken using the calibrated porous plasticity model. These simulations are then compared to the unit cell calculations in order to elucidate the differences between the various modelling strategies. The current study reveals that strain localization analyses using an imperfection band model and a spatially discretized unit cell are in reasonable agreement, while the bifurcation analyses predict higher strain levels at localization. Imperfection band analyses are finally used to calculate failure loci for the quadratic and the non-quadratic matrix yield surface under a wide range of loading conditions. The underlying matrix yield surface is demonstrated to have a pronounced influence on the onset of strain localization.

Keywords: Ductile failure; Unit cell; Porous plasticity; Strain localization; Bifurcation analysis; Imperfection band analysis; Third deviatoric stress invariant

1. Introduction

The loading paths exerted on arbitrarily positioned material elements in real structural components are rarely proportional (Dæhli et al., 2016). Metal alloys that have a face-centred cubic (FCC) crystal lattice, such as aluminium-based alloys, are known to display a curved yield surface (Hosford, 1972, 1996), thus imposing a dependence upon the third principal invariant of the stress deviator. The curvature of the yield surface is judged to influence the resulting plastic flow and deformation path, especially when the stress state is allowed to change throughout the loading stage. For instance, in the vicinity of a yield surface corner, rather small changes in the stress state may cause abrupt changes in the strain path of the material. This may in turn trigger localized deformations in the material body which either aids or initiates, and thus influence, the ductile failure process.

An abrupt change from a smoothly varying deformation path into a localized straining mode is a frequent observation for metal alloys subjected to large deformations. Such localization modes may result from small material non-uniformities, such as microvoid-containing bands, or from the decrease in work hardening and material softening of ductile solids when the plastic deformations are sufficiently large. Anand and Spitzig (1980) reported on incipient shear band formation even for positive, although small, work hardening levels in the case of plane deformation specimens under both tension and compression. But even if the material does not exhibit pronounced material softening, localized

*Corresponding author

Email address: lars.e.dahli@ntnu.no (Lars Edvard Bryhni Dæhli)

deformation may emerge due to a mismatch in material properties across some imperfection inside the material (Rudnicki and Rice, 1975; Rice, 1976; Needleman and Rice, 1978). If the imperfection contains a weaker material, which not necessarily holds true for any type of material but is assumed in the current study, the deformations will concentrate inside the band. Progression of the well-known ductile failure mechanism by void nucleation, growth and coalescence may then proceed rapidly inside the concentrated deformation zone which is why such strain localization phenomena are frequently used to define macroscopic failure.

Clausing (1970) conducted both uniaxial tension and plane strain tension experiments, and showed that ductility is markedly reduced in plane strain tension. This observation was also later supported by the experimental and numerical work of Hancock and Brown (1983). The difference in ductility between the plane strain and axisymmetric tension specimens was found to be around 70% for low-hardening steels, and only about 20% for high-hardening steels. This implies the dependence of work hardening on the strain localization process. Further, the triaxiality ratio is different in the two test specimens, and initially $\sim$ 70% higher in the plane strain tension specimen. The hydrostatic tensile stress may accordingly play a crucial role for the change in the ductility, since the stress triaxiality is known to greatly influence the ductile fracture strain (McClintock, 1968; Rice and Tracey, 1969; Hancock and Mackenzie, 1976; Koplik and Needleman, 1988; Hopperstad et al., 2003). However, a potential dependence of the yield function upon the deviatoric angle is also deemed important since the plane strain tension test corresponds to generalized shear while the uniaxial tension test corresponds to generalized tension.

Even though earlier studies had predicted a monotonously increasing fracture strain with decreasing stress triaxiality ratio, the experiments of Bao and Wierzbicki (2004) on an aluminium alloy displayed a non-smooth and non-monotonous evolution of the fracture strain with respect to the stress triaxiality ratio. Their study fuelled the idea of other decisive factors for ductile failure, possibly related to the deviatoric stress state. The dependence of the ductile failure strain upon the deviatoric stress state through the third deviatoric stress invariant, or the Lode parameter, was later demonstrated by the experimental work of Barsoum and Faleskog (2007a) using carefully designed double-notched tubular tension-torsion specimens made from Weldox steel alloys. Similar tension-torsion experiments using slightly different specimen geometries were later conducted by Haltom et al. (2013), Papasidero et al. (2014) and Scales et al. (2016). These studies unanimously demonstrate combined effects of the stress triaxiality and the Lode parameter on the equivalent strain at failure for ductile metal alloys. A noteworthy observation is that the fracture strain decreases with increasing triaxiality ratio for a given fixed Lode parameter. However, in tracing a plane stress path on the fracture locus this may lead to the non-monotonous evolution observed by Bao and Wierzbicki (2004) due to the Lode dependency. Also, the influence of the Lode parameter is greater for low triaxiality ratios, while it diminishes as the stress triaxiality increases for which the pronounced hydrostatic tensile stress facilitates ductile failure by void growth and coalescence.

The aforementioned studies, indicating the Lode dependence of ductile failure, were conducted under globally proportional loading conditions. There is however no guarantee that the local stress state where failure initiates corresponds to proportional loading, which is also indicated in the cited papers, and deviations from the global proportional path typically emerge well before failure initiates. Papasidero et al. (2015) have shown the effects of non-proportional loading paths in a hybrid experimental-numerical study on an aluminium alloy. The issue was also addressed in a recent paper by Gruben et al. (2017) in which the local loading paths were imposed in imperfection band analyses (Rice, 1976) either in a proportional or a non-proportional manner. Their results show prominent differences in the resulting failure strain. Moreover, recent unit cell studies (Benzerga et al., 2012; Dæhli et al., 2016; Thomas et al., 2016) elucidate that non-proportional loading paths greatly alter the onset of void coalescence, and thus the resulting ductility predictions, for the same strain-averaged state of stress. This implies that not necessarily all the differences obtained for the fracture strain in experiments can be attributed to the Lode parameter determined from the globally proportional loading path. One should consequently exert some caution in interpreting experimental results on a quantitative basis. To quantify the effects of the Lode parameter, detailed micromechanical studies using finite element unit cell models have been conducted under prescribed proportional states of stress (Barsoum and Faleskog, 2007b, 2011; Dunand and Mohr, 2014; Bomarito and Warner, 2015; Wong and Guo, 2015). These studies explicitly account for a shear deformation mode, and conditions are sought which minimize the resulting equivalent strain to failure. The numerical results clearly indicate that ductile failure is Lode dependent, which is now a well-established observation in the literature, and that stress states close to generalized shear generally yields lower ductility. This is in accord with the experimental studies using various test specimens. It should be noted that in the unit cell studies cited above, von Mises plasticity is assumed which does not display any intrinsic Lode effects. Thus, to study how the Lode dependence associated with the non-quadratic yield surface of the matrix material combine to the effects due to the

stress state is largely unexplored in terms of unit cell simulations. This serves as one of the motivations for the current investigation.

Recent experimental works of Morgeneyer et al. (2014, 2016) using compact-tension specimens made from aluminium alloys with low and high work hardening show that narrow bands of concentrated deformation form already at small deformations. They discuss that these strain bands could originate from heterogeneities of the material microstructure, which is plausible due to the discrete nature of polycrystals at this scale. Moreover, Morgeneyer et al. (2016) conducted two-dimensional plane strain simulations where soft zones were randomly positioned in the cross section of the test specimen to approximate a distribution of soft grains. These simulations displayed slant bands already at early loading stages which gives impetus to the idea of shear bands originating from material heterogeneities. However, they further argued that the regularity of the strain bands and their intermittent activity, which are captured by the soft zone model, imply that material heterogeneity is more unlikely, and the true source of the strain band emergence still remains to be disclosed. As reported in their paper, microvoids inside the band grow and rotate to align with the band orientation. But these effects were not detected before a rather large deformation was imposed which indicates the sequence of events for the ductile failure process. Although one should be cautious in extrapolating such experimental findings to arbitrary loading conditions, it seems that in some circumstances strain localization occurs prior to the ductile damage process. Ductile failure subsequently takes place inside the strain band due to void growth, rotation and shearing of the voids, and final coalescence along the band. Evidence that substantiates such observations was also provided by Tekoğlu et al. (2015) who studied this by means of finite element unit cell simulations under a wide range of proportional stress states. They report that void coalescence is preceded by strain localization on the macroscopic scale, which in their study was associated with the peak equivalent stress. This observation pertains to all the examined stress states reported in their study. However, the onset of strain localization and void coalescence was almost coincident for stress triaxialities below unity.

Even if the true origin of the localized strain bands is yet to be clarified, the recent findings of Morgeneyer et al. (2014, 2016) substantiate the use of imperfection band analyses in the spirit of Rice (1976) containing a voided band within the material. Since the band width is much greater than the characteristic dimensions associated with the microscopic voids (Morgeneyer et al., 2016), we may approximate this strain band as a dilutely voided band. To this end, porous plasticity models are employed to describe a material which exhibits damage softening due to the growth of microvoids. The Gurson model (Gurson, 1977) is widely used to model porous ductile solids and in its original form, it governs the macroscopic yielding of an aggregate of spherical voids embedded in an isotropic rigid-perfect plastic matrix governed by the J_2 flow theory. Previous studies (Hosford, 1972, 1996) have shown that many metal alloys frequently used in structural applications, which indeed includes aluminium alloys, are more accurately described by non-quadratic yield surfaces in which the magnitude of the stress state, defined by some tensor norm, changes with the deviatoric angle. Since this paper sets out to explicitly investigate such effects on the ductile failure predictions, and bearing in mind the analysis framework adopted, a suitable extension of the Gurson model including a dependence upon the third deviatoric stress invariant must be employed.

The Gurson model has been extended in a variety of ways over the past decades, see for instance a recent review paper by Benzerga et al. (2016). However, it seems that relatively few studies have been devoted to accounting for an isotropic non-quadratic matrix yield surface. Cazacu and Stewart (2009) included tension-compression asymmetry in the porous plasticity model using the same approach as Gurson (1977), which consequently introduces effects of the third deviatoric invariant, although in a slightly different form than that addressed in this paper. Later, a Tresca matrix description was included by Cazacu et al. (2014), but due to inherent difficulties arising in the homogenization problem, this model pertains only to axisymmetric loadings. Limitations to such stress states are too restrictive for the current application. Moreover, the yield surfaces for metal alloys are usually situated between the Tresca and the von Mises yield surfaces, and a more adequate matrix formulation should take this aspect into account. In the current work, we will adopt a heuristic approach to incorporate a Lode dependency in the Gurson framework. The resulting model follows along the same lines as the modification proposed by Doege and Seibert (1995) for a plastically anisotropic matrix. This extended version of the Gurson model was also recently used by Gruben et al. (2017). We note, however, that a usual assumption in the derivation of porous plasticity models, which was also used by Gurson (1977), is to disregard a coupling term (Cazacu and Stewart, 2009) between the deviatoric and mean strain rate components. This essentially renders the porous plasticity model on the same form as the one adopted in the current study. Recently, Soare (2016) and Benallal (2017) incorporated a matrix description governed by the Hershey yield criterion (Hershey, 1954; Hosford, 1972) in the upper-bound limit analysis of a hollow sphere. Soare (2016) derived an approximated macroscopic yield

function using a numerical approach, while Benallal (2017) obtained the yield criterion in a parametric form based on a rigorous upper-bound analysis.

The number of studies devoted to examine combined effects of the third deviatoric stress invariant and the hydrostatic stress using an extended porous plasticity model seems to be limited. Mear and Hutchinson (1985) investigated the onset of strain localization in dilutely voided solids for which kinematic hardening was included in the Gurson model. This introduces effects of yield surface curvature in the constitutive model which were shown to have a pronounced influence on the ductile failure strain, at least in the range of stress states employed in their calculations. Specifically, pure kinematic hardening led to a substantial decrease in the failure strain as compared to pure isotropic hardening. Similar investigations were undertaken by Tvergaard (1987) and Tvergaard and Van Der Giessen (1991), although these studies also extend the porous plasticity model to include effects of void nucleation and plastic spin, respectively. In agreement with the study of Mear and Hutchinson (1985), their results also demonstrate that the yield surface curvature affects the ductility with a purely kinematic hardening model leading to the lowest localization strain.

More studies have been devoted to bifurcation analyses and imperfection band analyses to address effects of either the Lode parameter or the hydrostatic stress separately. Yamamoto (1978) included an imperfection band with a material governed by the Gurson model and demonstrated the pronounced influence of introducing an imperfection rather than associating the localization strain to a bifurcation in the constitutive model. Needleman and Rice (1978) examined the ductility limits for a variety of constitutive models, both in the form of bifurcation and imperfection band analyses. In particular, they introduced vertex effects in the yield description by using the J_2 deformation theory, which are demonstrated to reduce the resulting failure strain estimates such that they are more in line with experiments. Furthermore, they employ the Gurson model inside the imperfection band, along similar lines as Yamamoto (1978), and provide numerical evidence for similar effects of including either vertex effects or dilatational effects inside the band material. They did not, however, combine the two effects. Also, they report numerical data which clearly show that, in the imperfection band analyses, similar trends can be obtained with various types of imperfections by tuning the imperfection parameters properly. This introduces some arbitrariness in the imperfection band analyses. In the present work, we believe that an imperfection band governed by the Gurson model is physically motivated by the experimental findings in Morgeneyer et al. (2014, 2016), at least on a qualitative basis. However, the strain localization analyses are known to be sensitive to the constitutive model, which must be properly validated in order to substantiate its use. An alternative is to explicitly resolve the approximated microstructure of the voided band material. This has been approached in a number of studies over the past two decades, initiated by the works of Barsoum and Faleskog (2007b). However, it seems that the recent work by Tekoğlu et al. (2015) is the only unit cell study that is in direct accordance with the imperfection band model of Rice (1976). Even though such models are superior in that they capture the true evolution of the voids, given an assumption of their initial size, shape and distribution, they are very costly in terms of computational time. For isotropic materials, in which the orientation of the imperfection band remains parallel with the intermediate principal stress direction, this may be tractable, but in the general case for anisotropic materials this still represents a major computational challenge.

The current paper intends to address effects of the yield surface curvature on strain localization in porous ductile solids. Non-quadratic yield functions are often employed to describe the homogenized material response of polycrystals and it is therefore of great importance to account for their effects on the predicted ductility. Further, we will address the calibration of a heuristic extension of the Gurson model from unit cell simulations that accurately describes an approximated microstructure of the porous material. Numerical calculations using a unit cell approach to the strain localization problem will be compared with bifurcation and imperfection band analyses. This work is purely based on a numerical approach, without any attempt to compare the results with experiments, and will treat a fictitious model material. As such, it does not give any quantitative predictions for strain localization, but it offers full control of the approximated material structure and the imposed stress state, which is crucial in order to assess the effects of varying the constitutive features of the material.

The paper is organized as follows. In Section 2, we present the stress state parameters that are used throughout the paper. Section 3 presents the constitutive relation for the matrix material. The evolution of the approximated material microstructure determined by numerical unit cell calculations is presented in Section 4. The porous plasticity model is described in Section 5 along with the calibration procedure. Strain localization analyses using both unit cell models and the bifurcation and imperfection band analyses are presented in Section 6. The paper is summarized in Section 7 with some concluding remarks.

2. Stress state description

We will impose various proportional stress states throughout these analyses. To ease this task, we define the stress state by some appropriate parameters. Let an arbitrary stress state, denoted P in Figure 1a, be expressed in the principal stress space with the principal stresses written as the sum of a deviatoric and hydrostatic part according to

$$\sigma_{\mathrm{I}} = \sqrt{\frac{2}{3}} r \cos(\theta) + \sigma_{\mathrm{h}} \tag{1a}$$

$$\sigma_{\mathrm{II}} = \sqrt{\frac{2}{3}} r \cos\left(\theta - \frac{2\pi}{3}\right) + \sigma_{\mathrm{h}} \tag{1b}$$

$$\sigma_{\mathrm{III}} = \sqrt{\frac{2}{3}} r \cos\left(\theta + \frac{2\pi}{3}\right) + \sigma_{\mathrm{h}} \tag{1c}$$

Here, $r = \sqrt{\boldsymbol{\sigma}' : \boldsymbol{\sigma}'} = \sqrt{2J_2}$ is the magnitude of the deviatoric stress state $\boldsymbol{\sigma}'$ in the deviatoric plane, $\sigma_{\mathrm{h}} = I_1/3$ is the hydrostatic stress, while θ is the deviatoric angle. Figure 1a shows an illustration of the principal stress space and Figure 1b shows a corresponding sketch of the deviatoric plane. The second principal deviatoric stress invariant and the first principal stress invariant are denoted J_2 and I_1, respectively. Note that the deviatoric angle is the angle spanned between the direction of the stress point and a projected base vector along the direction of σ_{I} in the deviatoric plane, as inferred from Figure 1b. Also, the principal stress components are assumed to be ordered according to $\sigma_{\mathrm{I}} \geq \sigma_{\mathrm{II}} \geq \sigma_{\mathrm{III}}$ which formally means that $0^\circ \leq \theta \leq 60^\circ$.

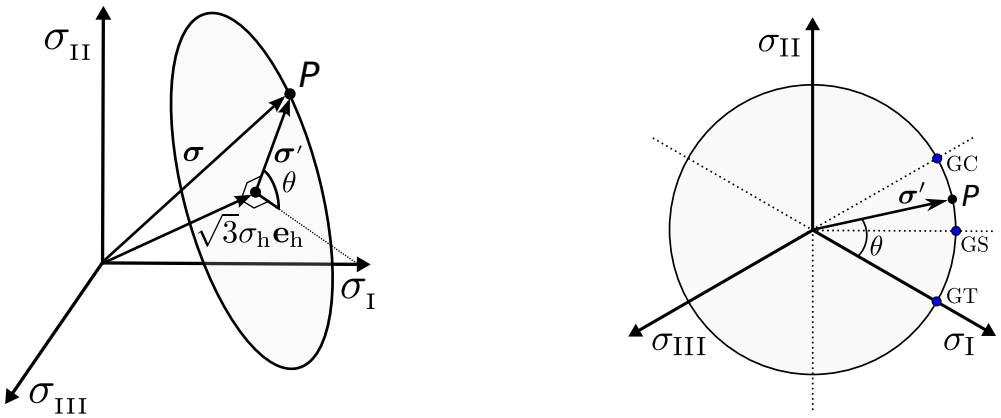

Figure 1: Illustration of a stress point P in (a) the principal stress space and (b) the deviatoric stress plane. The deviatoric and hydrostatic parts of the stress vector are indicated in the figure and the hydrostatic axis is denoted by $\mathbf{e}_{\mathrm{h}}$. The depicted ellipse, being a circle in the deviatoric plane, describes stress points with the same stress triaxiality ratio T. GT, GS, and GC refer to generalized tension, shear and compression, respectively.

In the following, we will use the stress triaxiality T and the Lode parameter L to govern the stress state. The stress triaxiality is defined from the hydrostatic stress σ_{h} and the equivalent von Mises stress $\sigma_{\mathrm{eq}}^{\mathrm{vm}}$ on the form

$$T = \frac{\sigma_{\mathrm{h}}}{\sigma_{\mathrm{eq}}^{\mathrm{vm}}} = \frac{I_1}{3\sqrt{3J_2}} \tag{2}$$

To describe the deviatoric stress state, the Lode parameter is defined as a ratio between the principal stress components which reads

$$L = \frac{2\sigma_{\mathrm{II}} - \sigma_{\mathrm{I}} - \sigma_{\mathrm{III}}}{\sigma_{\mathrm{I}} - \sigma_{\mathrm{III}}} \tag{3}$$

A relation between the Lode parameter and the third deviatoric stress invariant $J_3 = \det(\boldsymbol{\sigma}')$ is provided by the two

equations

$$L = \sqrt{3}\tan\left(\theta - \frac{\pi}{6}\right) \tag{4a}$$

$$\cos(3\theta) = \frac{3\sqrt{3}}{2}\frac{J_3}{\sqrt[3]{J_2}} \tag{4b}$$

From the definition of the Lode parameter, it follows that $L = -1$, 0, and 1 correspond to $\theta = 0°$, 30°, and 60°, respectively. From the above it is clear that the Lode parameter is not affected by the hydrostatic stress and is thus exclusively linked to the deviatoric stress state. We note that Lode parameters $L = -1$, 0, and 1 represent states of generalized tension (GT), shear (GS), and compression (GC), respectively, which will be often referred to throughout this paper.

3. Matrix constitutive formulation

The constitutive relations for the matrix material are formulated in a corotational framework. Hence, the corotated macroscopic stress $\hat{\boldsymbol{\sigma}}$ and rate-of-deformation $\hat{\mathbf{d}}$ tensors read

$$\hat{\boldsymbol{\sigma}} = \mathbf{R}^T \cdot \boldsymbol{\sigma} \cdot \mathbf{R} \tag{5a}$$

$$\hat{\mathbf{d}} = \mathbf{R}^T \cdot \mathbf{d} \cdot \mathbf{R} \tag{5b}$$

where $\boldsymbol{\sigma}$ and $\mathbf{d}$ are the Cauchy stress tensor and the rate-of-deformation tensor, respectively, referring to a fixed global basis. The orthogonal rotation tensor $\mathbf{R}$ defines the transformation between the local material basis and the fixed global basis. In the implicit finite element (FE) solver Abaqus/Standard, the corotational formulation corresponds to an update of the local basis using the material spin tensor $\mathbf{w}$ such that $\dot{\mathbf{R}} = \mathbf{w} \cdot \mathbf{R}$. The corotated elastic and plastic rate-of-deformation tensors, respectively $\hat{\mathbf{d}}^{\mathrm{e}}$ and $\hat{\mathbf{d}}^{\mathrm{p}}$, follow directly from the additive decomposition $\mathbf{d} = \mathbf{d}^{\mathrm{e}} + \mathbf{d}^{\mathrm{p}}$.

The elastic response is governed by the rate form of the generalized Hooke's law in terms of the corotated stress rate $\dot{\hat{\boldsymbol{\sigma}}}$ and the corotated elastic rate-of-deformation $\hat{\mathbf{d}}^{\mathrm{e}}$, namely

$$\dot{\hat{\boldsymbol{\sigma}}} = \frac{E}{1+\nu}\hat{\mathbf{d}}'^{\mathrm{e}} + \frac{E}{3(1-2\nu)}\mathrm{tr}\,(\hat{\mathbf{d}}^{\mathrm{e}})\mathbf{1} \tag{6}$$

where $\hat{\mathbf{d}}'^{\mathrm{e}}$ and $\mathrm{tr}\,(\hat{\mathbf{d}}^{\mathrm{e}})$ are respectively the deviatoric and volumetric parts of $\hat{\mathbf{d}}^{\mathrm{e}}$. The second order identity tensor is denoted by $\mathbf{1}$, the elastic constants E and ν refer to the elastic modulus and Poisson's ratio, respectively. The two elastic constants are listed in Table 1.

The plastic response is governed by a rate-independent plasticity formulation which incorporates effects of the third deviatoric stress invariant J_3. The yield function defining the interior and the periphery of the elastic domain reads

$$\phi\,(\hat{\boldsymbol{\sigma}}, p) = \sigma_{\mathrm{eq}}\,(\hat{\boldsymbol{\sigma}}) - \sigma_{\mathrm{M}}\,(p) \leq 0 \tag{7}$$

The equivalent stress is given by (Hershey, 1954; Hosford, 1972)

$$\sigma_{\mathrm{eq}}\,(\hat{\boldsymbol{\sigma}}) = \left(\frac{1}{2}\left[(\sigma_{\mathrm{I}} - \sigma_{\mathrm{II}})^m + (\sigma_{\mathrm{II}} - \sigma_{\mathrm{III}})^m + (\sigma_{\mathrm{I}} - \sigma_{\mathrm{III}})^m\right]\right)^{\frac{1}{m}} \tag{8}$$

in terms of the ordered principal stress components. The yield surface exponent m dictates the curvature of the yield surface. For FCC metals, such as aluminium-based alloys, a yield surface exponent value $m = 8$ is often employed (Hosford, 1996). In the current study, we will use the yield surface exponent values $m = 2$ and $m = 8$ to enforce a quadratic and a non-quadratic matrix yield surface, respectively. The corresponding yield surfaces are depicted in the deviatoric stress plane in Figure 2. We note that $m = 2$ renders the equivalent stress given by Equation (8) equal to the von Mises stress, and the matrix yielding is consequently not affected by the third deviatoric stress invariant J_3. The yield surface exponent $m = 8$ describes a yield surface lying in-between the Tresca and the von Mises yield surfaces, and is thus affected by the deviatoric angle.

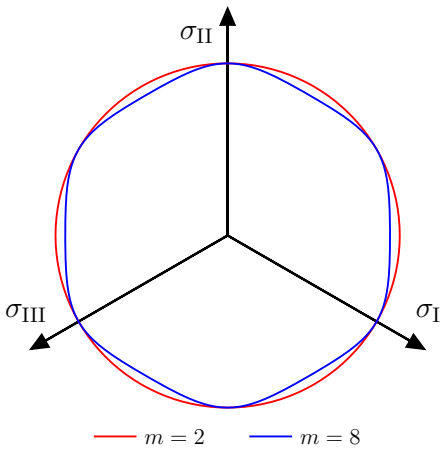

Figure 2: Yield surfaces for exponents $m = 2$ and $m = 8$ depicted in the deviatoric stress plane.

The matrix flow stress σ_{M} is governed by an isotropic work-hardening rule on the form

$$\sigma_{\mathrm{M}} = \sigma_0 + Q\left(1 - \exp\left(-Cp\right)\right) \tag{9}$$

where σ_0 denotes the initial yield stress, Q and C are material constants, and p is the accumulated plastic strain. The adopted values of the material parameters are purely generic, but deemed realistic parameters for low work-hardening aluminium alloys. These are listed in Table 1. The plastic strain rate is taken to be power conjugate to the matrix flow stress. Accordingly, the accumulated plastic strain is evaluated from

$$p = \int_0^t \dot{p}\,\mathrm{d}\bar{t} = \int_0^t \frac{\hat{\boldsymbol{\sigma}} : \hat{\mathbf{d}}^{\mathrm{p}}}{\sigma_{\mathrm{M}}}\,\mathrm{d}\bar{t} \tag{10}$$

where $\hat{\mathbf{d}}^{\mathrm{p}}$ is the corotated plastic rate-of-deformation tensor, defined by the associated flow rule as

$$\hat{\mathbf{d}}^{\mathrm{p}} = \dot{\lambda}\frac{\partial \phi\left(\hat{\boldsymbol{\sigma}}, p\right)}{\partial \hat{\boldsymbol{\sigma}}} = \dot{\lambda}\frac{\partial \sigma_{\mathrm{eq}}\left(\hat{\boldsymbol{\sigma}}\right)}{\partial \hat{\boldsymbol{\sigma}}} \tag{11}$$

Using the expression for plastic power and invoking the yield criterion $\phi\left(\hat{\boldsymbol{\sigma}}, p\right) = 0$, we obtain

$$\dot{w}^{\mathrm{p}} = \hat{\boldsymbol{\sigma}} : \hat{\mathbf{d}}^{\mathrm{p}} = \sigma_{\mathrm{eq}}\dot{\lambda} = \sigma_{\mathrm{M}}\dot{p} \quad \Rightarrow \quad \dot{\lambda} = \dot{p} \tag{12}$$

Note that we have used that $\sigma_{\mathrm{eq}}\left(\hat{\boldsymbol{\sigma}}\right)$ is a first order homogeneous function with respect to the stress tensor $\hat{\boldsymbol{\sigma}}$ to arrive at the second equality. The loading/unloading conditions are given by the relations

$$\phi \leq 0, \quad \dot{\lambda} \geq 0, \quad \phi\dot{\lambda} = 0 \tag{13}$$

Table 1: Generic material parameters used for the matrix material.

E [GPa]	ν	σ_0 [MPa]	Q [MPa]	C
70	0.3	100	100	10

A material user subroutine (UMAT) was employed to implement the constitutive relations in the finite element framework. The return map algorithm used herein is based on a semi-implicit update of the stress increment (Belytschko et al., 2000) in which the plastic moduli are not updated throughout the increment. To ensure accuracy of the

computations, we employed a substepping scheme in which the strain increment fed to the material subroutine was always kept smaller than a given tolerance value. For the matrix material, the strain increments were constrained by

$$\Delta t \sqrt{\hat{\mathbf{d}}' : \hat{\mathbf{d}}'} \leq 0.05 \frac{\sigma_0}{E} \tag{14}$$

where Δt is the time increment, and σ_0 and E are material parameters listed in Table 1.

4. Numerical calculation of the RVE response

The mechanical response of an approximate representative volume element (RVE) for the porous ductile solid is examined in this section by means of unit cell calculations. A brief overview of the model is given prior to an exposition of relevant results from the numerical simulations.

4.1. Unit cell model

The RVE is defined as a cube with a spherical centred void. Thus, we approximate the material microstructure by a uniform distribution of equally spaced spherical voids embedded in an isotropic Hershey matrix defined by the constitutive model outlined in Section 3. In the numerical simulations, we use the yield surface exponents $m = 2$ and $m = 8$, which offer the possibility to examine the effects of J_3 on the approximated microstructural behaviour governed by the unit cell response. The main purpose of these unit cell calculations is to evaluate the void growth for a variety of stress states using either a quadratic or a non-quadratic yield surface. To this end, the unit cell is loaded by the principal stress components, thus precluding any macroscopic shear stress. Symmetry conditions are further exploited by modelling only 1/8 of the entire RVE which significantly reduces the computational cost of the analyses. Figure 3a illustrates the chosen RVE and Figure 3b shows the corresponding discretized unit cell model.

Periodic and homogeneous boundary conditions are assigned to the unit cell by restricting the external boundaries to remain straight throughout the analyses, as required from symmetry considerations. Nonlinear kinematical constraints on the nodal displacements of the unit cell were utilized to control the imposed stress state. These were implemented by enforcing work equivalence in a fictitious node, and the degrees-of-freedom of that node are used to constrain the unit cell boundaries by the use of a Multi-Point Constraint (MPC) user subroutine. We will not outline the method in this section, as it is presented in a more general form in Section 6.1 and Appendix A. Also, the method is detailed in other studies, see for instance Faleskog et al. (1998), Kim et al. (2004), Wong and Guo (2015), Liu et al. (2016), or Dæhli et al. (2017). However, we note that this procedure allows the specification of a given macroscopic loading path and that proportional loading paths were imposed to the unit cell for which the stress triaxiality T and the Lode parameter L, as defined in Equations (2) and (3), were assigned prescribed values.

The initial unit cell geometry is given by the edge lengths $L_1 = L_2 = L_3 = 2\bar{L}$, where $\bar{L}$ is the dimension of the edges employed in the 1/8 model. For a spherical void, we have that $R_1 = R_2 = R_3 = \bar{R}$ and the initial void volume fraction is then defined by

$$f_0 = \frac{V_\mathrm{v}}{V_\mathrm{RVE}} = \frac{\pi}{6}\left(\frac{\bar{R}}{\bar{L}}\right)^3 \tag{15}$$

where V_v and V_RVE denote the volume of the void and the RVE, respectively. An initial void content of $f_0 = 0.005$ was utilized in all calculations. The chosen void volume fraction is deemed representative for the content of the primary void-nucleating particles in typical aluminium alloys (Westermann et al., 2014). We note that initial voids are assumed throughout this study, which is only a reasonable approximation under moderate and high stress triaxiality ratios and for a particle-matrix interface that is relatively weak. Both these assumptions are considered to be realistic for the materials and stress states employed herein.

Implicit FE simulations were conducted using Abaqus/Standard 6.13 (Abaqus, 2013). A mesh convergence study was carried out on beforehand to ensure a converged unit cell response. The details of that study is omitted here for the sake of brevity. Based on the mesh refinement study, we chose a unit cell configuration consisting of approximately 2000 linear 8-node solid elements. We employed selectively reduced integration (C3D8 in Abaqus) to reduce susceptibility towards volumetric locking of the finite elements, which could represent a numerical problem for the nearly incompressible matrix behaviour displayed under predominant plastic loading.

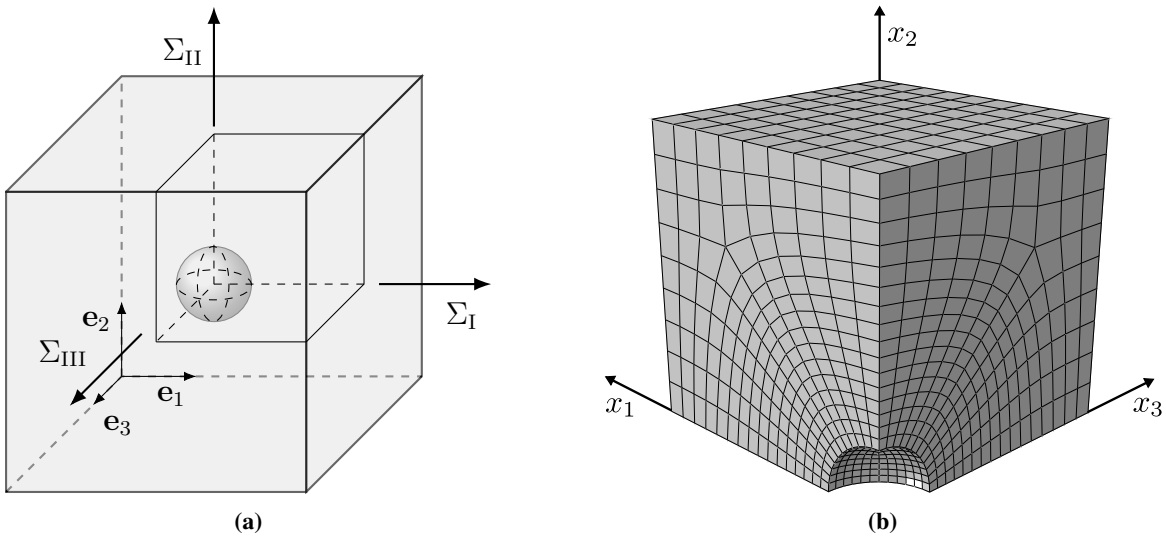

Figure 3: Illustration of the unit cell model showing (a) the adopted RVE, and (b) the spatially discretized FE model.

4.2. Unit cell results

In the current work, we prescribed proportional stress states governed by $T = 2/3$, 1, $5/3$, and 3 for which the Lode parameter was assigned five different values $L = -1, -1/2, 0, 1/2, 1$. Thus, a total number of 20 distinct stress states was considered for each yield surface exponent. Macroscopic response curves for the unit cell in terms of the equivalent von Mises stress $\Sigma^{\mathrm{vm}}_{\mathrm{eq}}$ and void volume fraction f are plotted in Figures 4 and 5 in the case of $m = 2$ and $m = 8$, respectively, against an equivalent von Mises strain given by

$$E^{\mathrm{vm}}_{\mathrm{eq}} = \sqrt{\frac{2}{3}\mathbf{E}' : \mathbf{E}'} \tag{16}$$

where $\mathbf{E}'$ denotes the deviatoric part of the macroscopic logarithmic strain tensor. These curves pertain to all the imposed stress states listed above. The range of stress states covered in the calculations is quite extensive, encompassing moderate to high levels of stress triaxiality and crossing the entire set of admissible Lode parameters. It should be duly noted that we have not included stress states in the low stress triaxiality range as this would lead to void collapse and render the unit cell analyses incompatible with the porous plasticity model to be presented in Section 5.

Figures 4a and 4b show results for the quadratic ($m = 2$) matrix description. From these numerical data it is apparent that, even in the case of a quadratic matrix yield surface, the Lode parameter affects the predicted unit cell response. This has been demonstrated in a number of studies throughout the literature (see for instance Zhang et al. (2001); Kim et al. (2004); Gao et al. (2010)). In particular, we should note the successive reduction in void growth rate as the Lode parameter increases which means that void growth is most rapid for $L = -1$ while it is slowest for $L = 1$. Thus, states of generalized tension promote rapid void growth leading to coalescence, while states of generalized compression prolongs the void growth process. This is related to the evolution of the void shape which is ellipsoidal in the general case, with the shape of the ellipsoid being dictated by the deviatoric stress state. However, such growth rate effects are diminishing with increasing levels of stress triaxiality, for which the influence of the stress deviator fades out, resulting in a nearly spherical void growth governed by the hydrostatic tensile stress. We also note that for the highest stress triaxiality, the void evolves into an oblate form rather than a prolate form even for generalized tension. This, admittedly somewhat anomalous, effect was first noticed by Budiansky et al. (1982) in an analytical treatment of an isolated spherical void embedded in a non-linear viscous material subjected to axisymmetric loading and was later observed in finite element unit cell calculations by Koplik and Needleman (1988) and Becker et al. (1989).

If we turn to the results for the non-quadratic ($m = 8$) matrix yield surface shown in Figures 5a and 5b, we observe even greater effects of the Lode parameter, and thus the third deviatoric principal stress invariant. In accordance with the results obtained using the quadratic yield surface, states of generalized tension give the most rapid void growth.

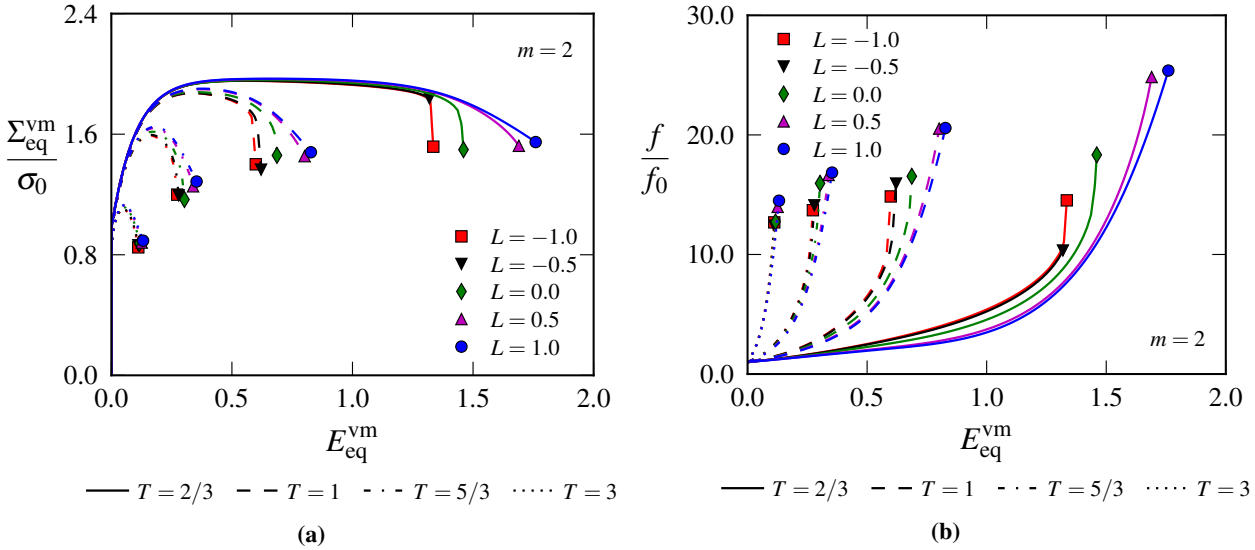

Figure 4: Unit cell results for the yield surface exponent $m = 2$ represented by (a) the equivalent stress and (b) the void growth plotted against the equivalent von Mises strain.

Also, the difference in the void growth between states of generalized tension and generalized compression are similar to what we observe for the quadratic yield surface, at least qualitatively. In fact, this is intuitive by inspection of the yield surfaces shown in Figure 2 since the deviatoric angles $\theta = 0°$ and $\theta = 60°$, or equivalently $L = -1$ and $L = 1$, exhibit the same stress magnitude and flow direction at yielding for both $m = 2$ and $m = 8$. Consequently, their global behaviour should to some extent be preserved when different yield surface exponents are imposed. However, by looking at Figures 5a and 5b, we infer that the void growth rate is not successively decreasing with increasing Lode parameter for the non-quadratic yield surface. The state of generalized shear gives the slowest void growth in this case, which is quite different from what we observe for the quadratic yield surface. Clearly, this must be related to matrix J_3 dependence since this is the only difference between the two sets of unit cell calculations. But to exactly predict how this Lode dependency will influence the macroscopic behaviour of the unit cell is quite challenging because the unit cell is also affected by the Lode parameter through the heterogeneity imposed by the void. The interplay between these two effects is not easily envisaged in advance and detailed numerical calculations like the unit cell simulations conducted herein are necessary to reveal their combined effect.

A potential explanation for the slower void growth in generalized shear for the non-quadratic yield surface has already been discussed by Steglich et al. (2010) and Shinohara et al. (2016) in the case of a plastically anisotropic matrix material. From Equation (2), we see that for any given triaxiality ratio T, the magnitude of the hydrostatic stress Σ_h is determined from the radius of the yield surface through

$$\Sigma_h = \Sigma_{eq}^{vm} T = \sqrt{\frac{3}{2}} r T \tag{17}$$

Hence, when the stress triaxiality is kept constant, the hydrostatic stress scales with the radius of the yield surface. When $m = 2$ or $m = 4$, the matrix yield surface reduces to a circle in the deviatoric plane, but for all other yield surface exponent values the matrix yield surface is dependent upon the deviatoric angle. This means that r will change according to the Lode parameter or the deviatoric angle, which is readily confirmed by inspecting the yield surfaces shown in Figure 2. In the case of the non-quadratic yield surface, r is smaller for generalized shear states than for generalized axisymmetric stress states. The hydrostatic stress consequently has a minimum for generalized shear loading ($L = 0$). Since the hydrostatic tensile stress is the main driving force for void expansion (Rice and Tracey, 1969), this could be the main reason for the rather large differences observed in the void growth between the quadratic and the non-quadratic yield surface.

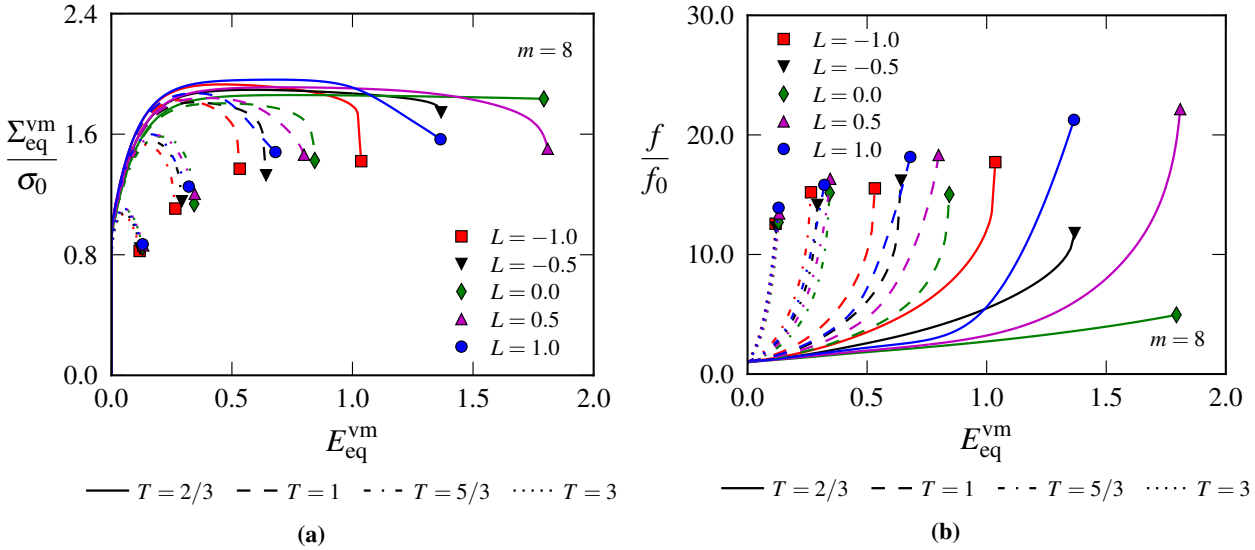

Figure 5: Unit cell results for the yield surface exponent $m = 8$ represented by (a) the equivalent stress and (b) the void growth plotted against the equivalent von Mises strain.

To investigate this matter in more detail, we define a new measure of stress triaxiality (Steglich et al., 2010; Shinohara et al., 2016) which accounts for the underlying matrix description, namely

$$T^* = \frac{\Sigma_h}{\Sigma_{eq}} = \frac{\Sigma_h}{\Sigma_{eq}^{vm}} \frac{\Sigma_{eq}^{vm}}{\Sigma_{eq}} = T \frac{\Sigma_{eq}^{vm}}{\Sigma_{eq}} \tag{18}$$

Keeping this ratio, rather than T, fixed in the unit cell simulations imposes the same external hydrostatic stress to the unit cell. Figure 6 compares the void growth in the case of generalized shear for the two different stress triaxiality definitions in the case of the two lower stress triaxialities. Results for the quadratic yield surface are also shown in the figure for comparison, but we note that the redefined stress triaxiality ratio T^* has no effect in this case since the radius of the yield surface is constant in the deviatoric plane. From the displayed results we find that the void growth rate is increased when T^* is employed, however not enough to conform with the void growth for the quadratic yield surface. This implies that there is another persistent source for the observed discrepancies in the void growth between $m = 2$ and $m = 8$.

Let us now turn to Figures 7a and 7b, which show comparisons between the porosity evolution using the quadratic (dashed lines) and the non-quadratic (solid lines) matrix yield surface in the case of $T = 2/3$ and $T = 3$, respectively, for generalized tension, shear, and compression states. We readily observe that the spread between the response curves for different Lode parameters is much more extensive for the non-quadratic yield surface, as displayed in Figure 7a for the lower triaxiality ratio. This is a manifestation of the combined J_3 effects due to the void shape evolution and the matrix description through the yield criterion. On the contrary, the influence of the J_3 parameter is essentially negligible for the high triaxiality value, although a bit more spread is observed for $m = 8$. This illustrates the dominant effect of the hydrostatic tension in these calculations, as seen from Figure 7b, which is far more protrusive than the deviatoric (J_3) effect induced by the matrix.

Before proceeding to the next section, another observation is definitely worth a remark. The numerical data presented throughout this section show that the quadratic matrix yield surface gives the most rapid void growth for generalized tension and that the void growth was successively decreasing with increasing Lode parameter. Although this trend is not displayed by the non-quadratic matrix yield surface, still the generalized tension state seems most favourable for void growth. This effect is even more prominent for the lower stress triaxiality ratios. Nahshon and Hutchinson (2008) introduced a shear modification of the Gurson model which has received considerable attention over the past years. Their model employs a void growth term that scales with the deviatoric angle, or the Lode parameter,

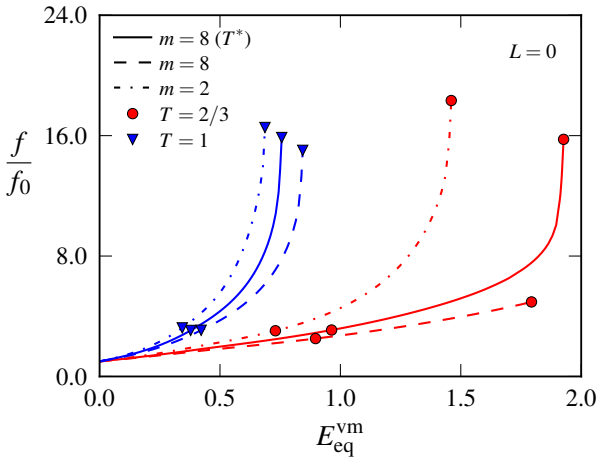

Figure 6: Comparison of void growth curves for the two triaxiality measures T and T^* at two levels of stress triaxiality. The plotted curves pertain to generalized shear states represented by the Lode parameter $L = 0$.

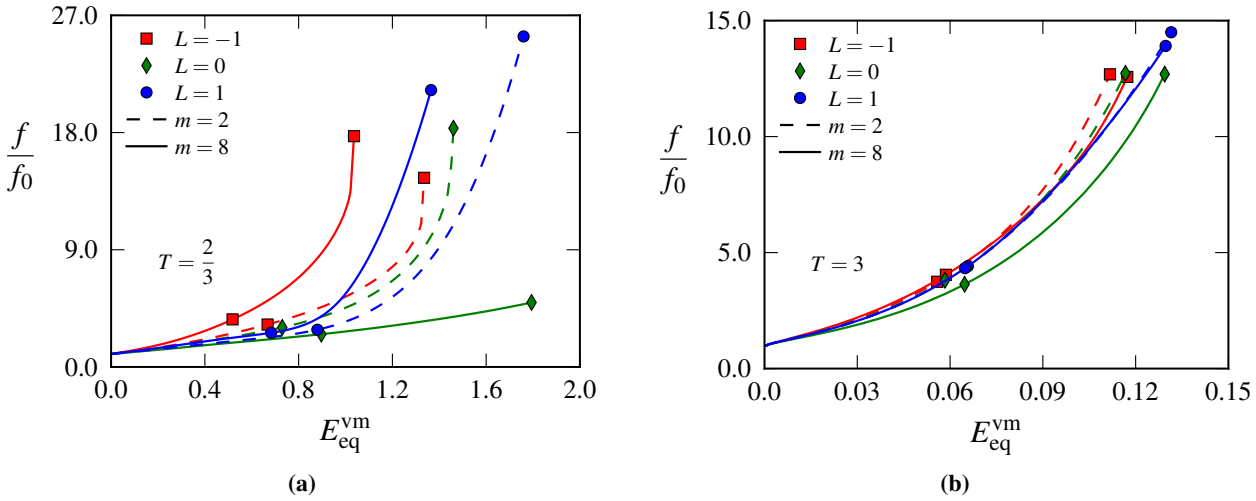

Figure 7: Comparison of void growth in simulations with $m = 2$ (dashed lines) and $m = 8$ (solid lines) for (a) $T = 2/3$ and (b) $T = 3$.

such that void growth is accelerated in generalized shear and unaltered in generalized tension and compression, the shape of the scaling being parabolic in terms of the Lode parameter. The unit cell calculations conducted in the present study suggest that such a shear modification should scale the void growth differently as a function of the Lode parameter since there is a large difference between generalized tension and generalized compression. This might serve as an appropriate remedy for the assumed spherical void growth in the Gurson model.

5. Porous plasticity model

The porous plasticity model (PPM) is presented in the following along with the calibration procedure and results from the calibration to unit cell data from the previous section. No attempt is made to derive rigorous upper-bound estimates in the spirit of the work by Gurson (1977) in the case of the PPM for a Hershey matrix description. To account for the influence of the third deviatoric stress invariant J_3 on the plastic yielding of the matrix, we rather modify the Gurson model heuristically by replacing the von Mises equivalent stress with the Hershey equivalent stress. Such modifications of porous plasticity models have been proposed previously in the literature (Doege and Seibert, 1995;

Bron and Besson, 2006; Besson, 2010; Steglich et al., 2010; Gruben et al., 2017) and is also used in a recent study by Dæhli et al. (2017).

5.1. Model formulation

The constitutive relations for the porous plasticity model are formulated in a corotational framework, as described for the matrix material in Section 3. The macroscopic corotated stress and rate-of-deformation tensors read

$$\hat{\mathbf{\Sigma}} = \mathbf{R}^T \cdot \mathbf{\Sigma} \cdot \mathbf{R} \tag{19a}$$

$$\hat{\mathbf{D}} = \mathbf{R}^T \cdot \mathbf{D} \cdot \mathbf{R} \tag{19b}$$

Capital letters are used in the following to designate homogenized tensor quantities that act on the material element. Further, an additive split of the macroscopic rate-of-deformation into elastic and plastic parts is assumed, such that $\hat{\mathbf{D}} = \hat{\mathbf{D}}^{\mathrm{e}} + \hat{\mathbf{D}}^{\mathrm{p}}$.

The yield function governing the homogenized response of the voided aggregate reads (Gurson, 1977; Tvergaard, 1981, 1982)

$$\Phi\left(\hat{\mathbf{\Sigma}}, \sigma_{\mathrm{M}}, f\right) = \left(\frac{\Sigma_{\mathrm{eq}}}{\sigma_{\mathrm{M}}}\right)^2 + 2q_1 f \cosh\left(\frac{3}{2} q_2 \frac{\Sigma_{\mathrm{h}}}{\sigma_{\mathrm{M}}}\right) - 1 - (q_1 f)^2 \leq 0 \tag{20}$$

where Σ_{eq} denotes the macroscopic Hershey equivalent stress in the form of Equation (8), and Σ_{h} is the macroscopic hydrostatic stress. As in the original Gurson model, f denotes the void volume fraction, and σ_{M} is the matrix flow stress governed by Equation (9) in the present formulation. The model parameters q_i were introduced by Tvergaard (1981) to obtain better correspondence to numerical results obtained with unit cell simulations, and these are determined in the calibration process.

The associated flow rule is adopted, such that the plastic part of the macroscopic rate-of-deformation is given by

$$\hat{\mathbf{D}}^{\mathrm{p}} = \dot{\Lambda} \frac{\partial \Phi}{\partial \hat{\mathbf{\Sigma}}} \tag{21}$$

where $\dot{\Lambda}$ is the plastic multiplier. An expression for the void growth rate is calculated from matrix incompressibility (Gurson, 1977)

$$\dot{f} = (1 - f)\,\mathrm{tr}\,(\hat{\mathbf{D}}^{\mathrm{p}}) \tag{22}$$

in which $\mathrm{tr}\,(\hat{\mathbf{D}}^{\mathrm{p}})$ coincides with the plastic volumetric rate-of-deformation. This relation is implicitly influenced by the Lode parameter, or equivalently J_3, due to the adopted equivalent stress measure and the yield criterion. The relation between the matrix equivalent plastic strain rate and the plastic multiplier is determined from the plastic power

$$\hat{\mathbf{\Sigma}} : \hat{\mathbf{D}}^{\mathrm{p}} = (1 - f)\,\sigma_{\mathrm{M}} \dot{p} \quad \Rightarrow \quad \dot{p} = \frac{\dot{\Lambda}}{(1 - f)\,\sigma_{\mathrm{M}}} \hat{\mathbf{\Sigma}} : \frac{\partial \Phi}{\partial \hat{\mathbf{\Sigma}}} \tag{23}$$

The elastic response is governed by the hypoelastic formulation given in Equation (6) which is assumed to be unaffected by the microscopic voids. This assumption is quite justified for the low content of voids that are typically found in commercial aluminium alloys, even more so since the elastic deformations are small when compared to their plastic counterparts. As for the matrix description used in the unit cell simulations, the elastic parameters and the material parameters governing the work-hardening rule are given in Table 1. Both yield surface exponents $m = 2$ and $m = 8$ are employed herein. The constitutive relations are completed by the loading/unloading conditions which are given by

$$\Phi \leq 0, \quad \dot{\Lambda} \geq 0, \quad \Phi \dot{\Lambda} = 0 \tag{24}$$

Temporal integration of the rate-constitutive equations was carried out using a semi-implicit return map algorithm (Belytschko et al., 2000) which was implemented using a UMAT subroutine in Abaqus/Implicit. A substepping scheme was employed to enforce sufficient accuracy of the integration procedure, and the strain increment fed to the material subroutine was constrained by

$$\Delta t \sqrt{\hat{\mathbf{D}} : \hat{\mathbf{D}}} \leq 0.05 \frac{\sigma_0}{E} \tag{25}$$

where Δt is the analysis time increment, and σ_0 and E are the material parameters listed in Table 1. Note that the total corotated rate-of-deformation tensor $\hat{\mathbf{D}}$ is used to define an effective strain increment, since the PPM is compressible. A numerical evaluation of the consistent tangent moduli was utilized due to the complexity associated with developing these moduli analytically.

5.2. Calibration

The optimization software LS-OPT (LS-OPT, 2017) is utilized to calibrate the PPM. To this end, the unit cell data obtained in Section 4.2 were used as target curves. In the optimization procedure, the Tvergaard parameters q_i were varied in order to obtain the best fit to the numerical data by the use of a sequential domain reduction algorithm. Residuals in both equivalent stress and void volume fraction as function of the equivalent strain were minimized in the calibration by the use of a least-square method. The optimized material parameters are listed in Table 2.

Table 2: Set of q_i parameters found from the optimization process.

m	q_1	q_2
2	1.426	0.853
8	1.449	0.857

Comparative curves between the unit cell model and the PPM are shown in Figure 8 in the case of $T = 2/3$ and $T = 5/3$. Figures 8a and 8b demonstrate that the PPM does not exhibit any J_3 dependency when the yield surface exponent is set to $m = 2$, which is recognized from the fact that all Lode parameters give exactly the same response. This corresponds to using the von Mises equivalent stress, for which the yield function in Equation (20) is known to lack the ability to display the Lode effects associated with the void shape evolution that are observed in the unit cell calculations. In the case of the non-quadratic matrix, we see from Figures 8c and 8d that the PPM is affected by the Lode parameter. However, the Lode dependency imposed by the Hershey equivalent stress measure is seen to induce symmetric response with respect to generalized tension and compression. This is consistent with the yield surfaces depicted in Figure 2, but not in line with the Lode dependence displayed in the unit cell simulations.

In terms of the stress-strain curves, see Figures 8a and 8c, we find that the void-induced softening is a bit too pronounced in the PPM for the low stress triaxiality ratios. This observation applies to both matrix descriptions, with the exception of $L = -1$ for the matrix with $m = 8$. By considering the corresponding void growth curves, this is quickly unravelled since the void growth is seen to be somewhat faster in the PPM up to rather large strains. The trend is opposite for the higher stress triaxiality ratio, where the void-induced softening in the PPM is less than in the unit cell calculations. This is related to the observation that the void growth is slower for the PPM for all the deviatoric stress states and yield surface exponents for the higher stress triaxialities, which prolongs the stable mechanical response phase and delays the onset of softening. When we employ q_i parameters different from unity, we deviate from the original Gurson model which is the exact solution in the hydrostatic limit. For the sets of q_i parameters listed in Table 2, the void growth rate is reduced as compared to the original Gurson parameters $q_1 = q_2 = 1$. This is the reason why the correspondence between the curves is deteriorated for increased traxiality levels. The fact that we are not able to obtain a set of q_i parameters that provides the same accuracy for all stress states implies that the PPM itself is not sufficiently refined to give an adequate representation to the approximated microstructure, meaning the unit cell calculations. The competition between the evolution of the void shape and the purely spherical void expansion is important in that regard, which might be remedied by using phenomenological extensions of the Gurson model (Nahshon and Hutchinson, 2008; Xue, 2008) or more advanced porous plasticity models that account for spheroidal and ellipsoidal void shapes (Gologanu et al., 1993; Madou and Leblond, 2012a,b) in the limit analysis.

We note that the values of the parameters obtained in the optimization process are largely dependent upon the stress states included in the calibration. If only the generalized tension analyses $L = -1$ are included, the resulting q_i parameters yield conservative estimates of the void growth. The opposite holds true if only $L = 1$ is considered. Since the employed PPM itself is not able to replicate the unit cell response for all stress states in terms of both void growth and equivalent stress, it can be argued that the q_i parameters should be calibrated from stress states that are most likely to be obtained in the application domain. Also, a potential remedy for some of the discrepancies observed in Figure 8 is to calibrate q_i for different Lode parameters separately, meaning that $q_i = q_i(L)$. We note that

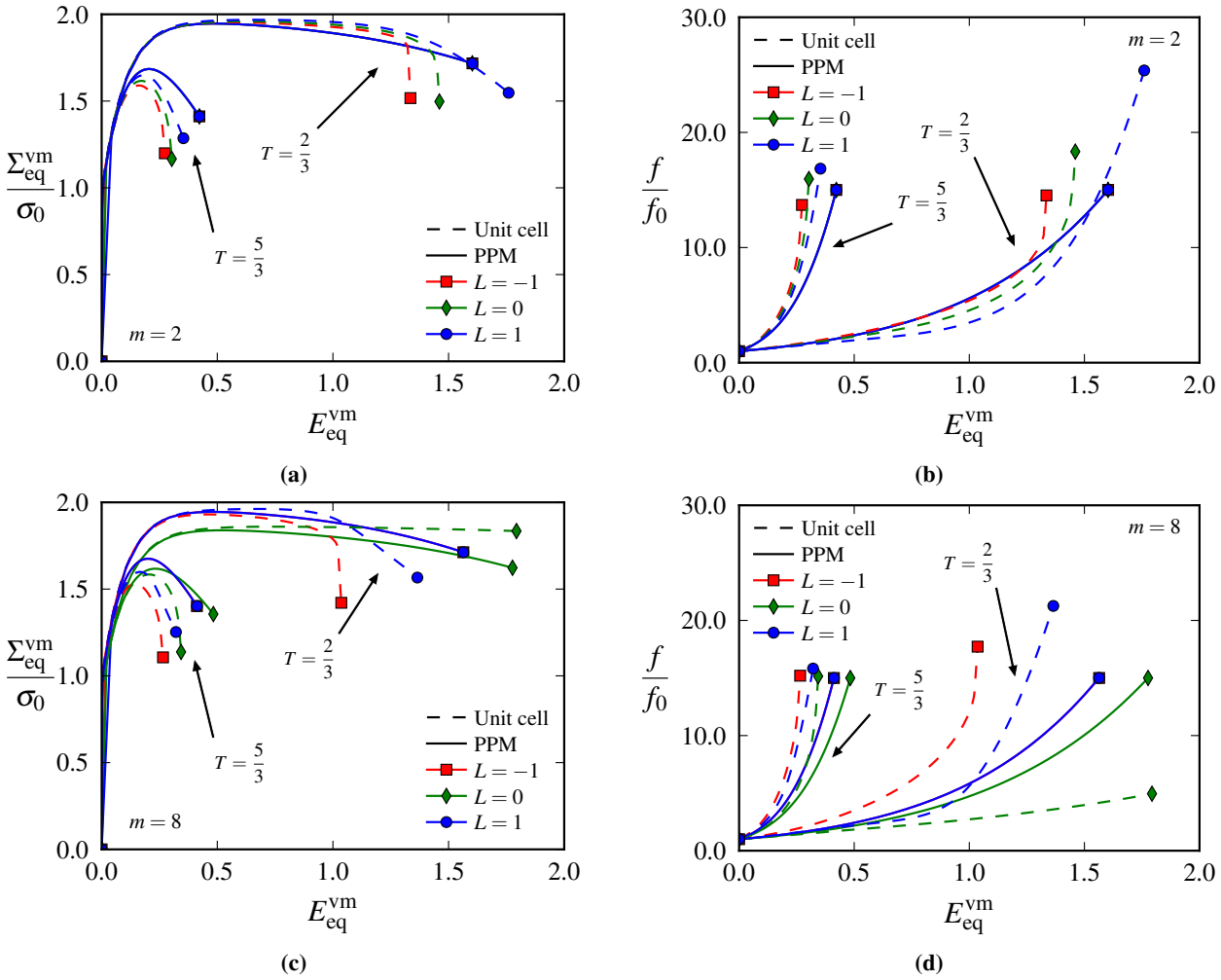

Figure 8: Comparison between results obtained with the unit cell (dashed lines) and the PPM (solid lines) with the optimized set of q_i parameters. The plotted curves pertain to generalized tension, shear, and compression, for stress triaxialities $T = 2/3$ and $T = 5/3$. Results are shown for both yield surface exponents (a,b) $m = 2$ and (c,d) $m = 8$.

this introduces a stress state dependency in the q_i parameters and it must be ensured that the plastic dissipation is non-negative. Previous studies in the literature (see for example Vadillo and Fernández-Sáez (2009) or Bomarito and Warner (2015)) have introduced a stress dependency in the q_i parameters to enhance the predictions of the Gurson model under non-proportional loading paths.

6. Strain localization analyses

Strain localization is in many cases a reliable indicator for when ductile failure occurs, since intense straining in a very constrained region is usually quickly followed by local crack initiation and propagation. In the following, we will employ three approaches to model strain localization. The first method is based on unit cell calculations in which a shear mode is included to account for band orientations that differ from the macroscopic principal stress directions. The second and third methods are based on bifurcation analysis and imperfection band analysis, respectively, following the work of Rice (1976). Both methods are presented separately in the first two subsections, while numerical results are presented and compared in the subsequent subsections. We note that the stress triaxiality ratios considered herein will be confined to $T \geq 2/3$. As briefly mentioned in Section 4.2, this choice is made since the Gurson model is better

suited for calculations in the range of intermediate and high stress triaxialities. However, low stress triaxialities are of great interest in the context of ductile failure and yield even greater effects of the Lode parameter.

6.1. Unit cell approach to strain localization analyses

To study strain localization by the use of unit cell simulations, we have employed a modelling framework that follows the treatments presented in Barsoum and Faleskog (2007b), Barsoum and Faleskog (2011), Dunand and Mohr (2014), and Wong and Guo (2015). A brief overview of the model and its finite element implementation in the implicit solver Abaqus/Standard are given in the following. We note that the purpose of conducting such unit cell analyses in the present study is to make comparisons to the more computationally efficient strain localization analyses for which the theoretical foundation is given by Rice (1976).

6.1.1. Unit cell model

It has been demonstrated in a number of studies that accounting for a shear deformation mode greatly influences the localization strain. Rudnicki and Rice (1975) and Perrin and Leblond (1993) showed that, for isotropic materials, localization will always occur in the plane parallel to the intermediate principal stress direction $\mathbf{n}_{\mathrm{II}}$. In order to facilitate such analyses, we prescribe an angle α between the major principal stress direction $\mathbf{n}_{\mathrm{I}}$ and the band unit normal $\mathbf{n}$. This angle is referred to as the band angle in the sequel. We note that in the current work, the band angle is kept constant throughout the loading, which is not in complete agreement with the framework of the imperfection band analysis. However, the difference induced by this fixation of the band orientation is deemed rather small in this range of triaxiality ratios, as also indicated by the results in Dunand and Mohr (2014) using both fixed and rotating bands. In the finite element model, the localization plane is taken to be parallel with the reference base vector $\mathbf{e}_3$, and thus $\Sigma_{33} = \Sigma_{\mathrm{II}}$ and $\Sigma_{13} = \Sigma_{23} = 0$. Figure 9a illustrates the governing problem in which the deformations localize in a narrow voided band.

To reduce the computational cost of the unit cell simulations, we have made use of the symmetry condition along the direction $\mathbf{n}_{\mathrm{II}}$ and only modelled half the unit cell. The initial unit cell geometry is then given by edge lengths equal to $L_1 = L_2 = \bar{L}$, while $L_3 = \bar{L}/2$. The radius of the void $\bar{R}$ is determined such that the corresponding void volume fraction has an initial value of $f_0 = 0.005$, in accordance with the porosity imposed in the unit cell simulations conducted previously. Homogeneous and periodic boundary conditions are imposed to the unit cell. The unit cell edges are thus subjected to the kinematic boundary conditions

$$u_1\left(\frac{\bar{L}}{2}, X_2, X_3\right) = u_1\left(-\frac{\bar{L}}{2}, X_2, X_3\right) + U_1 \tag{26a}$$

$$u_1\left(X_1, \bar{L}, X_3\right) = u_1\left(X_1, 0, X_3\right) + U_4 \tag{26b}$$

$$u_2\left(X_1, \bar{L}, X_3\right) = u_2\left(X_1, 0, X_3\right) + U_2 \tag{26c}$$

$$u_3\left(X_1, X_2, 0\right) = -\frac{U_3}{2} \tag{26d}$$

$$u_3\left(X_1, X_2, \frac{\bar{L}}{2}\right) = 0 \tag{26e}$$

where the displacement components U_i govern the homogeneous deformation and are illustrated in Figure 9b. In the finite element model, some nodes need to be constrained by imposing a zero displacement in order to prevent rigid body motion (see Figure 9b). The remaining nodes on the unit cell boundary are subjected to linear kinematic constraints to fulfil the periodicity requirement. In addition, the two unit cell edges with normal $\mathbf{e}_3$ are constrained to remain plane in accordance with the assumption that a material element inside the localization band will only develop in-plane shear stress components. More specifically, the middle section of the unit cell, which cuts through the void, defines a symmetry plane and is consequently fixed throughout the analyses. The opposing edge is prescribed the displacement $-U_3/2$ along the global base vector $\mathbf{e}_3$ such that the total displacement of the unit cell along $\mathbf{e}_3$ is U_3. An illustration of the unit cell model is presented in Figure 9b.

The volume averaged deformation gradient may be determined from

$$\mathbf{F} = \frac{1}{V_0}\int\limits_{V_0} \frac{\partial \mathbf{x}}{\partial \mathbf{X}}\,\mathrm{d}V_0 = \frac{1}{V_0}\int\limits_{S_0} \mathbf{x}\otimes\mathbf{n}_0\,\mathrm{d}S_0 \tag{27}$$

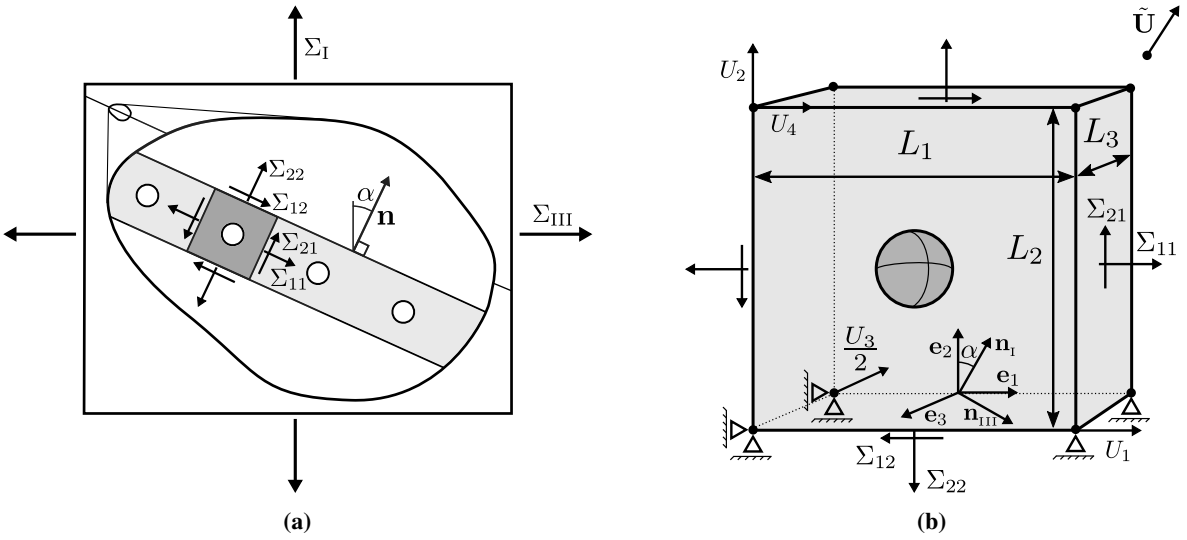

Figure 9: Unit cell model for strain localization into a narrow band. Figure (a) shows the governing strain localization problem with the principal stress components applied to a material block where a band of localized deformation emerges. The band orientation is indicated by the angle α and the band normal $\mathbf{n}$. Figure (b) illustrates the unit cell loading configuration of a material element located inside the presumed localization band. Boundary conditions are implied in the illustration. Note that a fictitious node is used to impose the appropriate boundary conditions defined by the displacement vector $\tilde{\mathbf{U}}$.

where $\mathbf{X}$ and $\mathbf{x}$ refer to material positions in the reference and current configurations, respectively, V_0 and S_0 are the volume and surface area in the reference configuration, and $\mathbf{n}_0$ is the unit surface normal of the unit cell boundaries in the reference configuration. The latter equality follows by the use of the gradient theorem. We employ a fixed Cartesian basis spanned by the base vectors $\mathbf{e}_i$ for both the reference and the current configurations. With reference to Figure 9b, the deformation gradient may be written on matrix form according to

$$[\mathbf{F}] = \begin{bmatrix} 1 + \dfrac{U_1}{L_1} & \dfrac{U_4}{L_2} & 0 \\ 0 & 1 + \dfrac{U_2}{L_2} & 0 \\ 0 & 0 & 1 + \dfrac{U_3}{L_3} \end{bmatrix} \tag{28}$$

All the macroscopic kinematic tensors presented in the following are evaluated from this volume averaged deformation gradient.

The macrosopic rate-of-deformation $\mathbf{D}$ of the unit cell is determined from the symmetric part of the velocity gradient $\mathbf{L} = \dot{\mathbf{F}} \cdot \mathbf{F}^{-1}$, such that

$$\mathbf{D} = \frac{1}{2}\left(\mathbf{L} + \mathbf{L}^T\right) = \frac{1}{2}\left(\dot{\mathbf{F}} \cdot \mathbf{F}^{-1} + \mathbf{F}^{-T} \cdot \dot{\mathbf{F}}^T\right) \tag{29}$$

For the current task, it is beneficial to recast $\mathbf{D}$ in vector form. Thus, we write

$$\{\mathbf{D}\} = \begin{Bmatrix} D_{11} \\ D_{22} \\ D_{33} \\ 2D_{12} \end{Bmatrix} = \left\{ \frac{\dot{U}_1}{l_1} \quad \frac{\dot{U}_2}{l_2} \quad \frac{\dot{U}_3}{l_3} \quad -\frac{U_4 \dot{U}_1}{l_1 l_2} + \frac{\dot{U}_4}{l_2} \right\}^T \tag{30}$$

where $l_i = L_i + U_i$ denote the current unit cell dimensions. This vector is further related to the global displacement

rates $\dot{U}_i$ applied to the unit cell boundaries via a linear transformation

$$\{\mathbf{D}\} = [\mathbf{T}]\{\dot{\mathbf{U}}\} = \begin{bmatrix} \frac{1}{l_1} & 0 & 0 & 0 \\ 0 & \frac{1}{l_2} & 0 & 0 \\ 0 & 0 & \frac{1}{l_3} & 0 \\ -\frac{U_4}{l_1 l_2} & 0 & 0 & \frac{1}{l_2} \end{bmatrix} \begin{Bmatrix} \dot{U}_1 \\ \dot{U}_2 \\ \dot{U}_3 \\ \dot{U}_4 \end{Bmatrix} \tag{31}$$

This relation will prove useful in the implementation of the MPC routine used to control the global stress state imposed to the unit cell. The details of this procedure are given in Appendix A.

The stress triaxiality T and Lode parameter L given in Equations (2) and (3), respectively, may be expressed uniquely in terms of the principal stress components. Further, we introduce principal stress ratios on the form

$$\psi_{\mathrm{II}} = \frac{\Sigma_{\mathrm{II}}}{\Sigma_{\mathrm{I}}} \quad \text{and} \quad \psi_{\mathrm{III}} = \frac{\Sigma_{\mathrm{III}}}{\Sigma_{\mathrm{I}}} \tag{32}$$

where $\psi_{\mathrm{III}} \leq \psi_{\mathrm{II}} \leq 1$ due to the ordering of the principal stress components. Using Equations (2) and (3), the stress triaxiality and Lode parameter may be written as functions solely of the principal stress ratios

$$T = \frac{1 + \psi_{\mathrm{II}} + \psi_{\mathrm{III}}}{3\sqrt{1 - \psi_{\mathrm{II}} - \psi_{\mathrm{III}} - \psi_{\mathrm{II}}\psi_{\mathrm{III}} + \psi_{\mathrm{II}}^2 + \psi_{\mathrm{III}}^2}} \tag{33a}$$

$$L = \frac{2\psi_{\mathrm{II}} - (1 + \psi_{\mathrm{III}})}{1 - \psi_{\mathrm{III}}} \tag{33b}$$

Thus, the prescription of T and L offers the ability to uniquely define the stress state in terms of the principal stress components. Note that Equation (33a) imposes a restriction on the major principal stress according to $\Sigma_{\mathrm{I}} > 0$. If we now solve Equation (33a) for ψ_{II}, insert this value into Equation (33b) and use the minimum of the two possible roots of the resulting expression for ψ_{III}, we find the inverse relations on the form

$$\psi_{\mathrm{II}} = \frac{1}{2}\left(\psi_{\mathrm{III}}\left(1 - L\right) + 1 + L\right) \tag{34a}$$

$$\psi_{\mathrm{III}} = \frac{9T^2\left(3 + L^2\right) + \left(9 - L^2\right) - 18T\sqrt{3 + L^2}}{9T^2\left(3 + L^2\right) - \left(3 - L\right)^2} \tag{34b}$$

Although T and L uniquely defines the principal stress state, given in terms of the principal stress components Σ_i and the corresponding principal directions $\mathbf{n}_i$, the stress components in the plane spanned by base vectors $\mathbf{e}_1$ and $\mathbf{e}_2$ may take on an infinite number of values depending upon the band angle α. To express the relation between the principal stress space and the stress state in the reference basis spanned by the unit vectors $\mathbf{e}_i$, we employ the angle α between the major principal stress component Σ_{I} and the stress component Σ_{22}. Further, we define a set of stress ratios ρ_i between the stress components Σ_{ij} on the form

$$\rho_2 = \frac{\Sigma_{22}}{\Sigma_{11}}, \quad \rho_3 = \frac{\Sigma_{33}}{\Sigma_{11}}, \quad \rho_4 = \frac{\Sigma_{12}}{\Sigma_{11}} \tag{35}$$

With reference to Figure 9b, we note that the principal directions are given by the unit vectors

$$\mathbf{n}_{\mathrm{I}} = \begin{Bmatrix} \sin\alpha \\ \cos\alpha \\ 0 \end{Bmatrix}, \quad \mathbf{n}_{\mathrm{II}} = \mathbf{e}_3 = \begin{Bmatrix} 0 \\ 0 \\ 1 \end{Bmatrix}, \quad \mathbf{n}_{\mathrm{III}} = \begin{Bmatrix} \cos\alpha \\ -\sin\alpha \\ 0 \end{Bmatrix} \tag{36}$$

Thus, the stress tensor may be expressed in both the global basis $\mathbf{e}_i$ and the principal basis $\mathbf{n}_k$ such that

$$\boldsymbol{\Sigma} = \Sigma_{ij}\mathbf{e}_i \otimes \mathbf{e}_j = \sum_{k=\mathrm{I}}^{\mathrm{III}} \Sigma_k \mathbf{n}_k \otimes \mathbf{n}_k \tag{37}$$

By performing the transformation from the principal stress space into the reference basis of the unit cell, we obtain a relation between the stress components Σ_{ij} and the principal stress components Σ_k. This may be conveniently expressed in matrix form as

$$[\boldsymbol{\Sigma}] = \begin{bmatrix} \Sigma_{\mathrm{I}} \sin^2\alpha + \Sigma_{\mathrm{III}} \cos^2\alpha & (\Sigma_{\mathrm{I}} - \Sigma_{\mathrm{III}}) \cos\alpha \sin\alpha & 0 \\ (\Sigma_{\mathrm{I}} - \Sigma_{\mathrm{III}}) \cos\alpha \sin\alpha & \Sigma_{\mathrm{I}} \cos^2\alpha + \Sigma_{\mathrm{III}} \sin^2\alpha & 0 \\ 0 & 0 & \Sigma_{\mathrm{II}} \end{bmatrix} \tag{38}$$

Introducing the principal stress ratios defined in Equation (32), the stress components applied to the unit cell are further expressed in terms of Σ_{I}, ψ_{II}, and ψ_{III} according to

$$\Sigma_{11} = \left(\sin^2\alpha + \psi_{\mathrm{III}} \cos^2\alpha\right) \Sigma_{\mathrm{I}} \tag{39a}$$

$$\Sigma_{22} = \left(\cos^2\alpha + \psi_{\mathrm{III}} \sin^2\alpha\right) \Sigma_{\mathrm{I}} \tag{39b}$$

$$\Sigma_{33} = \psi_{\mathrm{II}} \Sigma_{\mathrm{I}} \tag{39c}$$

$$\Sigma_{12} = \cos\alpha \sin\alpha \left(1 - \psi_{\mathrm{III}}\right) \Sigma_{\mathrm{I}} \tag{39d}$$

Thus, we may finally determine the stress ratios ρ_i, given by Equation (35), as functions of the principal stress ratios ψ_i and the angle α

$$\rho_2 = \frac{\cos^2\alpha + \psi_{\mathrm{III}} \sin^2\alpha}{\sin^2\alpha + \psi_{\mathrm{III}} \cos^2\alpha} \tag{40a}$$

$$\rho_3 = \frac{\psi_{\mathrm{II}}}{\sin^2\alpha + \psi_{\mathrm{III}} \cos^2\alpha} \tag{40b}$$

$$\rho_4 = \frac{\cos\alpha \sin\alpha \left(1 - \psi_{\mathrm{III}}\right)}{\sin^2\alpha + \psi_{\mathrm{III}} \cos^2\alpha} \tag{40c}$$

6.1.2. Controlling the macroscopic loading path

We first note that Equations (40a)-(40c) combined with Equations 34a and 34b give the opportunity to prescribe the stress ratios ρ_i for given values of the stress triaxiality T, Lode parameter L, and band angle α. This enable us to control the macroscopic stress state imposed to the unit cell by some suitable numerical procedure.

In order to control the average state of stress imposed to the unit cell, it was proposed by Faleskog et al. (1998) to transform the stress state of the unit cell into a hypothetical space in which a uniaxial state of stress prevails. This is realized by introducing a new set of degrees-of-freedom to which the boundary conditions are imposed, and then drive the deformation of the unit cell by appropriate nonlinear kinematic constraints. These degrees-of-freedom are incorporated through a fictitious node, as shown in Figure 9b, and the nonlinear kinematic constraints are enforced through an MPC user subroutine in Abaqus/Standard. We have reviewed this procedure in Appendix A in the case of four displacement components, which reduces to the method used in Section 4 when $\alpha = 0°$ or $\alpha = 90°$. An interpretation of the degrees-of-freedom involved in the constraints is provided in Figure 9b. For other expositions of the method, the reader is referred to Barsoum and Faleskog (2007b, 2011), Dunand and Mohr (2014), or Wong and Guo (2015).

6.1.3. Localization indicators

To determine the onset of strain localization, a localization indicator is often taken on the form (Needleman and Tvergaard, 1992; Barsoum and Faleskog, 2007b, 2011; Dunand and Mohr, 2014)

$$\xi_{\mathrm{F}} = \frac{||\dot{\mathbf{F}}_{\mathrm{b}}||}{||\dot{\mathbf{F}}_{\mathrm{o}}||} >> 1 \tag{41}$$

where $||\dot{\mathbf{F}}_{\mathrm{b}}||$ and $||\dot{\mathbf{F}}_{\mathrm{o}}||$ are tensor norms of the time derivative of the deformation gradient. With reference to Figure 9a, the norm $||\dot{\mathbf{F}}_{\mathrm{b}}||$ corresponds to the rate of the deformation gradient across the assumed band, while $||\dot{\mathbf{F}}_{\mathrm{o}}||$ is the rate of the deformation gradient outside the assumed band where the deformation is homogeneous. The latter reduces towards zero as the strains localize and the localization indicator then approaches infinity. This is an appropriate definition of strain localization in the imperfection band analyses. To evaluate the rate of the deformation gradient inside and outside the imperfection band in the unit cell simulations, we extracted the nodal displacements u_1 and u_2 from the yellow and red nodes in Figure 10. The yellow nodes were used to calculate the deformation gradient across the band, while the red nodes were used to approximate the deformation gradient outside the imperfection band. We note that the deformation along base vector $\mathbf{e}_3$ is uniform due to the imposed symmetry condition, and the corresponding component of the deformation gradient F_{33} is then identical inside and outside the imperfection band.

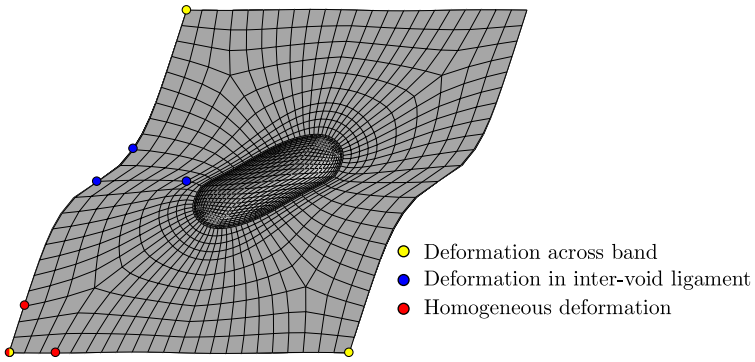

Figure 10: Overview of the nodes that are used to extract the displacement information needed to evaluate localization criteria ξ_{F} and ξ_{D}.

The localization criterion based on ξ_{F} is not always reliable in the unit cell simulations because the displacement at the unit cell boundaries across the band may be relatively uniform even if the void has expanded to such a degree that void coalescence is unavoidable. This is a prominent observation for generalized compression states, defined by $L = 1$, where the voids might be found to nearly impinge the unit cell edges but still not trigger localization as defined from Equation (41). We employed a localization criterion according to $\xi_{\mathrm{F}} > 5$ in the current study. The value of ξ_{F} is quite influential on the predicted failure strain for generalized compression states, and some stress states may accordingly not give strain localization using this localization criterion.

In an attempt to account for even more local measurements, which presumably triggers the localization criterion also for generalized compression, we define an alternative localization indicator on the form

$$\xi_{\mathrm{D}} = \frac{||\mathbf{D}_{\mathrm{l}}||}{||\mathbf{D}_{\mathrm{o}}||} >> 1 \tag{42}$$

Here, $||\mathbf{D}_{\mathrm{l}}||$ denotes an effective rate-of-deformation calculated from the average deformation gradient inside the intervoid ligament while $||\mathbf{D}_{\mathrm{o}}||$ is the effective rate-of-deformation evaluated from the deformation gradient in the homogeneously deformed region outside of the band. This may be interpreted as a criterion based on the averaged strain rate between adjacent voids located inside the assumed imperfection band. The nodal displacements of the blue nodes in Figure 10 are used to calculate $\mathbf{D}_{\mathrm{l}}$, while the displacements of the red nodes are used to evaluate $\mathbf{D}_{\mathrm{o}}$. We note that this criterion will be sensitive to small changes in the nodal displacements inside the ligament since it is averaged only over a small region which is quite heavily deformed. Also, it is highly mesh dependent, which requires more

attention from the user. In the present study, we chose a localization indicator value of $\xi_{\mathrm{D}} > 5$.

Inspired by the work of Wong and Guo (2015) and Liu et al. (2016), we also employed a third localization indicator in the current work. Instead of being defined in terms of kinematic nodal quantities, which are presumably quite influenced by the mesh refinement, this localization criterion is based on energy considerations. Thus, localization is governed by both stress and strain quantities of the unit cell volume, and is not as mesh dependent as the two other localization indicators defined by Equations (41) and (42). The macroscopic elastic and plastic deformation power contributions are given by

$$\dot{W}_{\mathrm{d}}^{\mathrm{e}} = \int_V \boldsymbol{\sigma} : \mathbf{d}^{\mathrm{e}} \, \mathrm{d}V \tag{43a}$$

$$\dot{W}_{\mathrm{d}}^{\mathrm{p}} = \int_V \boldsymbol{\sigma} : \mathbf{d}^{\mathrm{p}} \, \mathrm{d}V \tag{43b}$$

By introducing the ratio between the elastic and the plastic work rate, we use the localization indicator on the form (Wong and Guo, 2015; Liu et al., 2016)

$$\xi_{\mathrm{W}} = \frac{\dot{W}_{\mathrm{d}}^{\mathrm{e}}}{\dot{W}_{\mathrm{d}}^{\mathrm{p}}} \tag{44}$$

Strain localization is in the current work defined as $\xi_{\mathrm{W}} = 0$, which implies a state of neutral loading (Wong and Guo, 2015). Due to the time discretization, this criterion is not expected to be exactly satisfied, and we have then used the first negative value. We also note that this criterion matches the predictions of Equations (41) and (42) rather well for some loading situations. However, it is generally more conservative, but also more readily evaluated for states of generalized compression.

We note that other localization criteria may also be used. For instance, Tvergaard (2012) and Bomarito and Warner (2015) used the peak stress as an indicator for when failure will occur. In the paper by Tekoğlu et al. (2015), they defined macroscopic localization from the point of maximum equivalent stress, while localization due to void coalescence was defined as the instant when the ratio between maximum and minimum plastic strain rate at the void surface first exceeded a threshold value. The variety of localization indicators used throughout the literature indicates that there is still no consensus on how to define the point of failure.

6.2. Imperfection band approach to strain localization

The framework of the strain localization analyses presented herein was set by Rice (1976). We will use the porous plasticity model proposed in Section 5 with the q_i parameters determined in Section 5.2 to govern the dilutely voided material with an initial porosity of $f_0 = 0.005$. An illustration of the model is shown in Figure 11. In this paper we will conduct analyses both in the sense of a bifurcation in the porous plasticity model, for which the material is everywhere the same, and using an initial non-uniformity where the material outside the band reduces to the Hershey material description. A recent paper by Gruben et al. (2017) has employed the same implementation of the imperfection band analysis as the one used herein to investigate strain localization in sheets made from two advanced high-strength steels.

Compatibility requirements entail that the displacements only vary with the coordinate $\bar{X} = \mathbf{X} \cdot \mathbf{n}_0$ in the direction of the band normal across the imperfection band. The rate of the deformation gradient inside the band then reads (Rice, 1976; Needleman and Rice, 1978)

$$\dot{\mathbf{F}}_{\mathrm{b}} = \dot{\mathbf{F}}_{\mathrm{o}} + \dot{\mathbf{q}}_0 \otimes \mathbf{n}_0 \tag{45}$$

where $\dot{\mathbf{F}}_{\mathrm{o}}$ is the rate of the deformation gradient imposed to the bulk material, $\dot{\mathbf{q}}_0$ denotes the rate of the deformation non-uniformity across the band and $\mathbf{n}_0$ denotes the band normal in the reference configuration. In the case of a pure shear band $\dot{\mathbf{q}}_0$ is orthogonal to the normal $\mathbf{n}_0$ whereas for a purely dilatational band it is parallel.

From Equation (45) it is understood that the difference in stress rate between the inside and the outside of the imperfection band is only a function of the $\bar{X}$-coordinate along the normal direction $\mathbf{n}_0$. Thus, in the reference configuration, continuing a state of equilibrium requires that

$$\mathbf{n}_0 \cdot \dot{\mathbf{N}}_{\mathrm{b}} = \mathbf{n}_0 \cdot \dot{\mathbf{N}}_{\mathrm{o}} \tag{46}$$

where $\dot{\mathbf{N}}_\mathrm{b}$ and $\dot{\mathbf{N}}_\mathrm{o}$ are the nominal stress rates inside and outside the band, respectively. Equations (45) and (46) are the two governing equations of the imperfection band model, in addition to the constitutive laws that describe the material response to deformation. These may just as well be formulated in the current configuration using the spatial kinematic and kinetic tensors, as for instance done in the work by Yamamoto (1978). In the following, we will formulate the equations in an updated reference configuration (updated Lagrangian description) which is taken to instantaneously coincide with the current configuration (Nahshon and Hutchinson, 2008; Haddag et al., 2009). Note that this is entirely equivalent to a formulation in the current configuration, as shown by Rudnicki and Rice (1975).

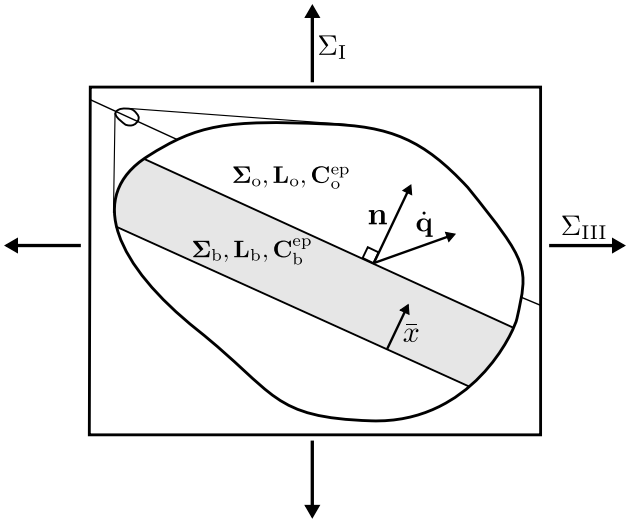

Figure 11: Illustration of the imperfection band model representing a weak discontinuity in the otherwise uniformly deformed material. Quantities with subscript "o" denote the material outside of the imperfection band, whereas quantities with subscript "b" refer to the material inside the band.

In the updated Lagrangian formulation, the compatibility condition expressed by Equation (45) is formulated in terms of the velocity gradient $\mathbf{L}$, such that

$$\mathbf{L}_\mathrm{b} = \mathbf{L}_\mathrm{o} + \dot{\mathbf{q}} \otimes \mathbf{n} \tag{47}$$

and the connection between the rate of the nominal and Cauchy stress tensors reduces to

$$\dot{\mathbf{N}} = \dot{\boldsymbol{\Sigma}} - \mathbf{L} \cdot \boldsymbol{\Sigma} + \mathrm{tr}\,(\mathbf{L})\,\boldsymbol{\Sigma} \tag{48}$$

The objective Jaumann stress rate $\overset{\nabla\mathrm{J}}{\boldsymbol{\Sigma}}$ is used to define the rate-constitutive equations

$$\overset{\nabla\mathrm{J}}{\boldsymbol{\Sigma}} = \mathbf{C}^\mathrm{ep} : \mathbf{D} = \mathbf{C}^\mathrm{ep} : \mathbf{L} \tag{49}$$

where $\mathbf{C}^\mathrm{ep}$ is the elasto-plastic tangent stiffness (Needleman et al., 1992). The time derivative of the Cauchy stress may then be written in terms of the Jaumann stress rate according to

$$\dot{\boldsymbol{\Sigma}} = \overset{\nabla\mathrm{J}}{\boldsymbol{\Sigma}} + \mathbf{W} \cdot \boldsymbol{\Sigma} - \boldsymbol{\Sigma} \cdot \mathbf{W} \tag{50}$$

Substituting this expression in Equation (48) yields

$$\dot{\mathbf{N}} = \overset{\nabla\mathrm{J}}{\boldsymbol{\Sigma}} - \mathbf{D} \cdot \boldsymbol{\Sigma} - \boldsymbol{\Sigma} \cdot \mathbf{W} + \mathrm{tr}\,(\mathbf{L})\,\boldsymbol{\Sigma} \tag{51}$$

Inserting Equation (49) and using the relations $2\mathbf{D} = \mathbf{L} + \mathbf{L}^T$ and $2\mathbf{W} = \mathbf{L} - \mathbf{L}^T$ gives

$$\dot{\mathbf{N}} = \mathbf{C}^{\mathrm{ep}} : \mathbf{L} - \frac{1}{2}\left(\mathbf{L} + \mathbf{L}^T\right) \cdot \boldsymbol{\Sigma} - \frac{1}{2}\boldsymbol{\Sigma} \cdot \left(\mathbf{L} - \mathbf{L}^T\right) + \mathrm{tr}\left(\mathbf{L}\right)\boldsymbol{\Sigma} \tag{52}$$

The nominal stress rate may then be rewritten

$$\dot{\mathbf{N}} = \mathbf{C}^{\mathrm{t}} : \mathbf{L} \tag{53}$$

where

$$C^{\mathrm{t}}_{ijkl} = C^{\mathrm{ep}}_{ijkl} - \frac{1}{2}\left(\Sigma_{ik}\delta_{jl} + \delta_{ik}\Sigma_{jl} + \delta_{il}\Sigma_{jk} - \Sigma_{il}\delta_{jk}\right) + \Sigma_{ij}\delta_{kl} \tag{54}$$

and δ_{ij} denotes the Kroenecker delta.

Equation (46) is now given by

$$\mathbf{n} \cdot \mathbf{C}^{\mathrm{t}}_{\mathrm{b}} : \mathbf{L}_{\mathrm{b}} = \mathbf{n} \cdot \mathbf{C}^{\mathrm{t}}_{\mathrm{o}} : \mathbf{L}_{\mathrm{o}} \tag{55}$$

Using Equation (55) in combination with Equation (47), this is recast in its final form

$$\left(\mathbf{n} \cdot \mathbf{C}^{\mathrm{t}}_{\mathrm{b}} \cdot \mathbf{n}\right) \cdot \dot{\mathbf{q}} = \mathbf{n} \cdot \left(\mathbf{C}^{\mathrm{t}}_{\mathrm{o}} - \mathbf{C}^{\mathrm{t}}_{\mathrm{b}}\right) : \mathbf{L}_{\mathrm{o}} \tag{56}$$

Strain localization is defined by $\det\left(\mathbf{n} \cdot \mathbf{C}^{\mathrm{t}}_{\mathrm{b}} \cdot \mathbf{n}\right) = 0$, which implies that $\dot{\mathbf{q}}$ is not uniquely defined. We note that the bifurcation case is retrieved when $\mathbf{C}^{\mathrm{t}}_{\mathrm{b}} = \mathbf{C}^{\mathrm{t}}_{\mathrm{o}}$ and the problem is then reduced to solving the equation

$$\det\left(\mathbf{n} \cdot \mathbf{C}^{\mathrm{t}} \cdot \mathbf{n}\right) = 0 \tag{57}$$

where $\mathbf{C}^{\mathrm{t}}$ is the tangent operator governing the constitutive response (see Equation (53)). The velocity non-uniformity $\dot{\mathbf{q}}$ is evaluated by the use of a fixed-point iteration procedure whenever $\det\left(\mathbf{n} \cdot \mathbf{C}^{\mathrm{t}}_{\mathrm{b}} \cdot \mathbf{n}\right) > 0$. Details regarding the numerical implementation are given in a paper by Morin et al. (2017).

In the numerical analyses, the velocity gradient outside the imperfection band $\mathbf{L}_{\mathrm{o}}$ is prescribed such that the stress triaxiality T and the Lode parameter L are kept fixed to prescribed levels. Details regarding this procedure may be found elsewhere in the literature, see for instance Nahshon and Hutchinson (2008) or Dæhli et al. (2017). Both the quadratic ($m = 2$) and the non-quadratic ($m = 8$) matrix yield surface descriptions are employed. In the case of the bifurcation analyses presented in Section 6.4, the material both inside and outside the imperfection band corresponds to the porous plasticity model presented in Section 5 with an initial porosity of $f_0 = 0.005$. In conjunction with the imperfection band analyses presented in Section 6.4 and 6.5, all calculations are performed with a material imperfection governed by the porous plasticity model using an initial porosity of $f_0 = 0.005$ inside the band. In the imperfection band analyses, the material outside the band is sound and thus $f = 0$ in the bulk material.

6.3. Strain localization predictions with the unit cell approach

Unit cell simulations were conducted for a range of proportional stress states to examine differences between a quadratic and a non-quadratic matrix yield surface on strain localization. Specifically, we imposed stress states corresponding to stress triaxialities $T = 2/3$, 1, $5/3$, and 3 for generalized shear states $L = 0$. We also ran simulations with the Lode parameters $L = \pm 1, \pm 3/4, \pm 1/2$, and $\pm 1/4$ for a stress triaxiality of $T = 1$. A number of band orientations α were used to estimate a minimum failure strain for a given stress state. However, due to the computational demand associated with these simulations, we set the minimum difference between two successive band angles to $\Delta\alpha = 2.5^\circ$ and the exact minimum of the failure strain is consequently not likely to be captured. The results are, however, deemed to be quite close to the "true" minimum obtained from a very refined band resolution since the differences between failure strain values in the proximity of the critical orientation were found to be rather small. This may be inferred from Figure 12.

The failure strain values obtained with the energy-based localization criterion, defined by $\xi_{\mathrm{W}} = 0$ in Equation (44), are shown in Figure 12 against the imposed band angle for a Lode parameter $L = 0$. Figure 12a pertains to $T = 2/3$ and 1, whereas Figure 12b corresponds to $T = 5/3$ and 3. These analyses imply that strain localization occurs in a direction close to 45° for the two lowest stress triaxiality levels regardless of the yield surface exponent, whereas the angle of the localization band is somewhat lower for the higher triaxialities. The latter observation implies a transition

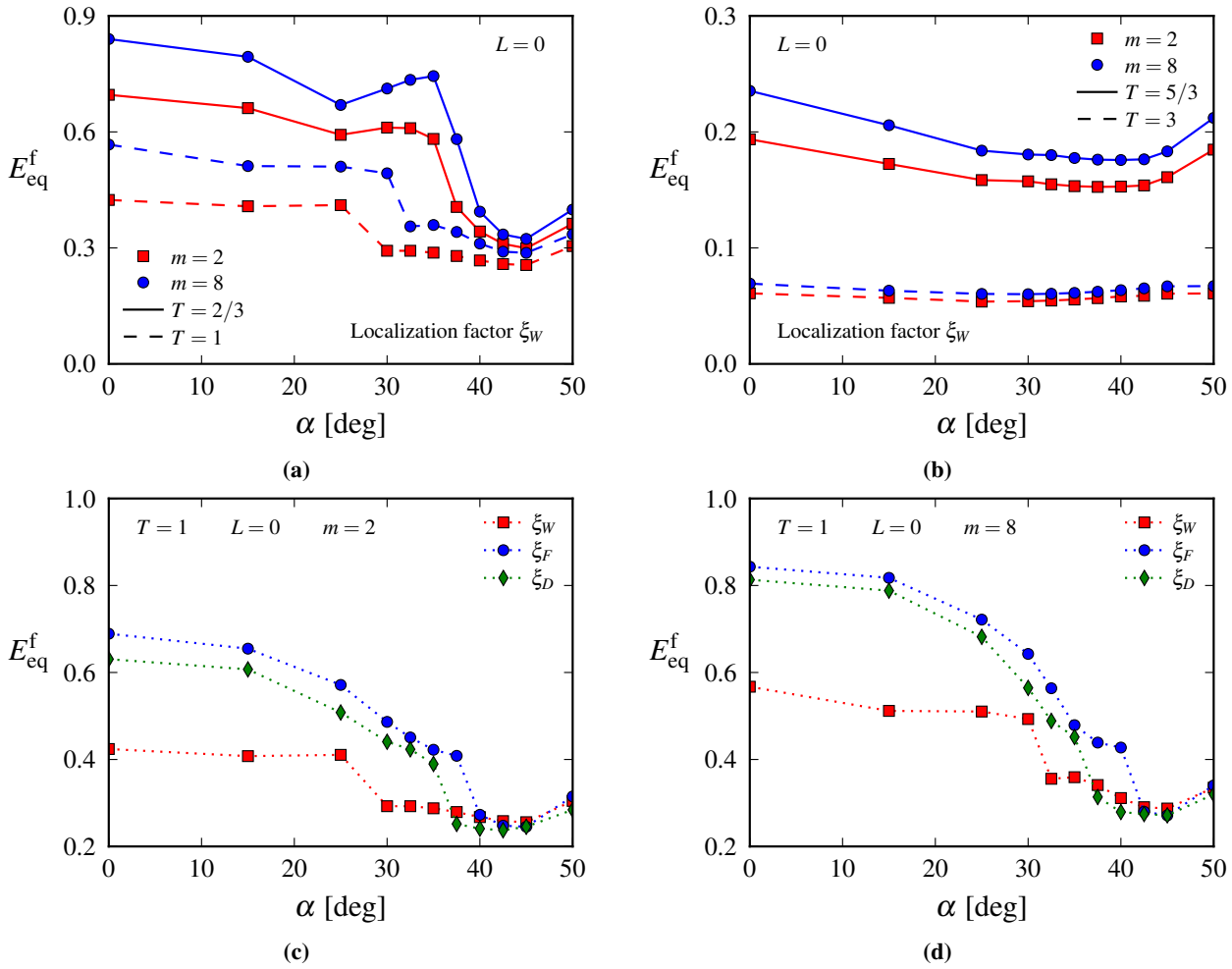

Figure 12: Failure strain values under generalized shear for different band orientations α imposed to the unit cell in the finite element calculations. Comparisons between quadratic and non-quadratic matrix yield surfaces are made for (a) the lower stress triaxialities and (b) the higher stress triaxialities. Localization predictions using the three different indicators are shown in (c) for $m = 2$ and (d) for $m = 8$ for stress states governed by $T = 1$ and $L = 0$.

from shear-dominated failure to a failure mode governed by void growth and coalescence as the stress triaxiality ratio is increased. Also, since nearly all the examined orientations α yield roughly the same failure strain level for the highest stress triaxiality, this implies that increasing triaxiality leads to a more diffuse localization mechanism due to the arbitrariness of the band inception. The band formation is then presumably more progressive and an increased amount of damage softening can be sustained after the onset of localization and prior to material failure. This is substantiated by the numerical analyses conducted by Tekoğlu et al. (2015), for which the onset of strain localization and void coalescence are seen to coincide only for $T < 1$ whereas the onset of coalescence is increasingly delayed for higher T. Under such circumstances the difference between strain localization at the macroscopic level, as captured by the model framework of Rice (1976), and the more local process of void coalescence seems more prominent.

Another observation worth a remark is that the strain at localization is lower for the quadratic yield surface than for the non-quadratic counterpart in the case of generalized shear loading ($L = 0$). This is somewhat contradictory to what is reported in the literature (Needleman and Rice, 1978; Mear and Hutchinson, 1985; Tvergaard, 1987; Tvergaard and Van Der Giessen, 1991), where a higher curvature of the yield surface usually expedites localization. To the best knowledge of the authors, this effect seems largely unexplored in the literature using unit cell calculations. If we consider the differences obtained in terms of the void growth in Section 4.2 for generalized shear (see Figure 7a), this

result may follow from intuition since accelerated void growth is judged favourable for early failure. A potential reason for this observation was discussed in Section 4.2 based on the difference in radius of the yield surface between the two yield surface exponents. Since this difference is at its peak for generalized shear, and we in these calculations use the triaxiality ratio defined in Equation (2), the resulting macroscopic hydrostatic stress for $m = 8$ is lower than for $m = 2$ by a few percent. We refer to Figure 2 to see the differences between the two yield surfaces.

A comparison between the failure strain levels using the three different localization indicators for a loading state $T = 1$ and $L = 0$ have been included in Figures 12c and 12d. We see that either of the three localization indicators are generally in good agreement in terms of the critical band orientation, which means that they all predict the same failure mode. It is also seen that the magnitude of the failure strain varies more with the band angle for indicators ξ_{F} and ξ_{D} than for the energy-based indicator ξ_{W}. However, it should be noted that for the critical band orientation, the three localization indicators more or less coincide under the given loading condition ($T = 1$ and $L = 0$).

Figure 13a shows equivalent stress-strain curves (blue lines) and porosity-strain curves (red lines) for the critical band orientation $\alpha_{\mathrm{c}} = 35^{\circ}$ in the case of a stress state corresponding to $T = 1$ and $L = -1$. Three deformed configurations of the finite element model are shown in the Figures 13b and 13c for each of the two yield surface exponents $m = 2$ and $m = 8$, respectively, to give an indication of the void shape and size at the various localization predictions. We observe a pronounced difference between the failure strain levels obtained using the three different localization indicators for this stress state. The energy-based indicator seems overly conservative in terms of ductile failure prediction under the given stress state. However, it matches very well with the onset of macroscopic softening, which is also an instability associated with loss of uniqueness. These results demonstrate that ductility predictions are in general highly sensitive to the indicator which is used even if the failure mode, defined by the critical orientation α_{c}, is similar. This is important to keep in mind if such analysis methodologies are to be used for material characterization and determination of failure loci. An interesting observation is that all localization indicators predict instability when the void content is rather low ($f_{\mathrm{c}} \sim 2\% - 4\%$).

Before we proceed with a comparison between the unit cell, the bifurcation analyses, and the imperfection band analyses, we note that the results presented in Figures 12 and 13a show that the quadratic matrix yield surface gives the lowest failure strain for the generalized shear states $L = 0$, while the opposite holds true for the generalized tension state $L = -1$. Thus, we observe a change in whether the quadratic or the non-quadratic matrix yield surface gives the lowest failure strain depending on the Lode parameter. The ductile failure process is indeed Lode dependent (see for example Barsoum and Faleskog (2007a,b)) and the intrinsic J_3 dependency of the matrix material interplays with the Lode effects emerging due to the spatial heterogeneity introduced by the void and the void shape evolution. Again, we turn to the void growth curves to find a potential explanation for this behaviour. From Figure 7a, we readily see that the void growth is more rapid for $m = 8$ than for $m = 2$ when $L = -1$, while the opposite holds true for $L = 0$. We also alluded to a pronounced influence of the Lode parameter on the void growth in Section 4.2. The same observation is made from the unit cell simulations of the band model for the generalized tension state, as seen from the porosity-strain curves shown in Figure 13a. This is one of the reasons why the ductility is reduced for $m = 8$ under generalized tension. We will come back to this observation when discussing results from the imperfection band analyses. However, the argumentation is then somewhat different.

6.4. Comparison between the different modelling strategies

To the best knowledge of the authors, direct comparisons of unit cell calculations with bifurcation and imperfection band analyses are yet not available in the literature. However, many studies employing either the former (Barsoum and Faleskog, 2007b, 2011; Dunand and Mohr, 2014; Bomarito and Warner, 2015; Wong and Guo, 2015) or the latter (Rudnicki and Rice, 1975; Rice, 1976; Yamamoto, 1978; Needleman and Rice, 1978; Mear and Hutchinson, 1985; Tvergaard, 1987) line of approach have previously been conducted. But considering the computational expense associated with the unit cell simulations, it is of great interest to make quantitative comparisons to the bifurcation and imperfection band analyses, which are of much less computational demand. To get an idea of the difference in computational time, one unit cell simulation takes about 1 hour running in parallel on 12 CPUs. Approximately 10 band angles must be imposed to determine the critical band angle with decent accuracy. This number multiplied by the number of investigated stress states amounts to roughly 5 days of continuous computation for each yield surface exponent using the unit cell approach. In comparison, strain localization analyses using the bifurcation or imperfection band models are conducted in a few minutes with a much higher resolution of the imposed band angles. The use of imperfection band analyses thus reduces the effort associated with generating failure loci that subsequently can

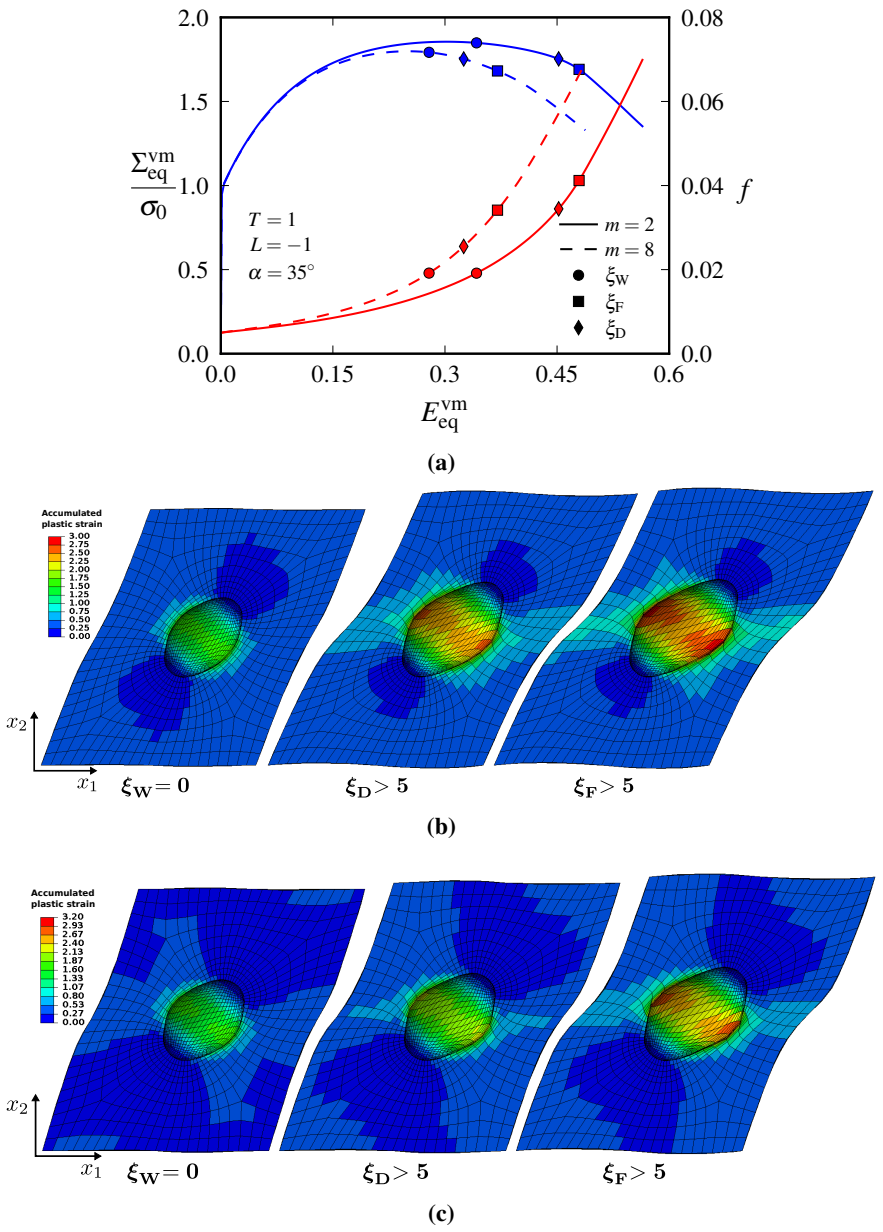

Figure 13: Unit cell results for $T = 1$ and $L = -1$ at the critical band angle $\alpha_c = 35°$. Equivalent stress-strain (blue) and porosity-strain (red) curves are shown in (a), while deformed configurations of the unit cell are shown for (b) $m = 2$ and (c) $m = 8$ with fringes of accumulated plastic strain at the analysis step corresponding to failure using the three different localization indicators.

be used to calibrate and validate numerical models for ductile failure to be used in full-scale simulations. Also, we can potentially gain more insight into the critical conditions for ductile failure since a much greater range of loading conditions can be examined. This argument seems even more important for plastically anisotropic solids where the critical band is arbitrarily oriented in space, and no *a priori* assumption of alignment with the intermediate principal stress direction can be made. At this point, however, we must assess the predictive capabilities and limitations of the employed constitutive model, since this influences the failure strain predictions - more so for the bifurcation analysis than for the imperfection band analysis. In fact, Needleman and Rice (1978) showed that relatively similar results can be obtained using various imperfection band materials by a suitable tuning of the constitutive parameters, the most

decisive factor being the introduction of the imperfection itself.

Figure 14 compares numerical results from various imposed stress states using imperfection band analyses and unit cell simulations. Results from bifurcation analyses are included in Figures 14a and 14b, showing the failure strain as function of the stress triaxiality ratio for generalized shear. The bifurcation analyses always provide the upper bound to the failure strain and are seen to give fairly high estimates of the failure strain when compared to the imperfection band analyses and the unit cell calculations. It has been previously reported (Rice, 1976; Needleman and Rice, 1978; Yamamoto, 1978) that, even with a constitutive formulation accounting for damage softening, strain localization predictions based on bifurcation analyses greatly overestimate the ductility. Further, the agreement between the imperfection band analyses and the unit cell calculations for the generalized shear states is remarkable. This holds true for all the localization indicators, which are more or less conforming, as was also indicated by the results presented in Figure 12c and 12d. We note that the conformity between the unit cell calculations and the imperfection band analyses is somewhat deteriorated for the higher triaxialities, and it seems that as the hydrostatic stress starts to dominate, the unit cell predictions are actually approaching those of the bifurcation analyses. Now, we should remark that a bifurcation of the homogenized material model is highly susceptible to variations in the constitutive parameters, for example q_i in the yield function given by Equation (20). These parameters were calibrated from unit cell simulations conducted for a large number of stress triaxialities and Lode parameters, and the goodness-of-fit between the porous plasticity model and the unit cell varies for each stress state, as indicated by the curves in Figure 8. Moreover, the porous plasticity model as it stands is not capable of accounting for void shape effects, which are obviously inherent to the unit cell model. Effects of void-induced softening under shear loadings can be heuristically included in the Gurson model, see for instance Nahshon and Hutchinson (2008). Also, Gurson-type models that incorporate general ellipsoidal voids, thus including effects of void shape and also orientation by some suitable update of the principal void axes, have been published (Madou and Leblond, 2012a,b). Attempts to assess the influence of such extensions on the strain localization are not pursued in the current work.

Turning to the results for $T = 1$ and varying the Lode parameter, shown in Figures 14c and 14d, we find that the Lode parameter is quite influential for the agreement between the unit cell calculations and the imperfection band analyses. In the range of biaxial tension, meaning positive Lode parameters $L > 0$, the failure strains evaluated from the bifurcation approach are inaccurate. We consequently restrict the discussion to results from the imperfection band analyses in the following. The difference between the localization predictions for the unit cell model using the three indicators is seen to greatly vary with the Lode parameter. For stress states close to generalized shear, the three indicators are quite similar and in close agreement with the imperfection band analyses. For stress states in the vicinity of the two generalized axisymmetric states $L = \pm 1$, the difference is more pronounced and the localization indicator ξ_{W} yields the most conservative estimates of the ductility. This observation is most prominent for loading conditions close to generalized compression $L \approx 1$. Also, the variation with the Lode parameter is not qualitatively similar to the imperfection band analyses using ξ_{W} as the criterion for failure. The failure loci from the unit cell model are brought in closer agreement to the imperfection band model if either of the two indicators ξ_{F} and ξ_{D} are employed. In these cases, the unit cell results are qualitatively similar to the imperfection band analyses in the sense that they are more affected by the Lode parameter. A comment worthwhile in this respect is that ξ_{D} is quite sensitive to the value chosen to define localization, which is set to $\xi_{\mathrm{D}} > 5$ in the current work, and that it also depends upon the mesh size used in the intervoid ligament. Since this indicator compares an equivalent strain rate evaluated in the region between adjacent voids to the equivalent strain rate in the homogeneously deformed region, it may trigger localization prior to the energy-based criterion which intuitively should set the limit for when localization can possibly occur. As such, the corresponding results should be interpreted with some caution. However, the use of ξ_{D} gives an indication of localization within the unit cell due to excessive void growth and subsequent coalescence when the global deformation of the unit cell otherwise suppresses a macroscopic instability. This scenario is encountered for generalized compression states using the stress triaxiality ratios investigated herein. This is elucidated by the results in Figure 14c where $L = 1$ does not permit the indicator ξ_{F} to be evaluated. It can of course be discussed whether such a stress state can be referred to as having an instability, but it will nonetheless lead to void coalescence which inevitably causes macroscopic crack formation and fracture.

Although some differences persist between the unit cell simulations and the imperfection band analyses, they are indeed rather similar from a qualitative point-of-view. The motivation for comparing the two modelling approaches resides in the qualitative results, and we do not intend nor expect them to exactly conform. However, judging by the results in Figure 14, the imperfection band analyses seem to capture the unit cell response rather well. We will then use

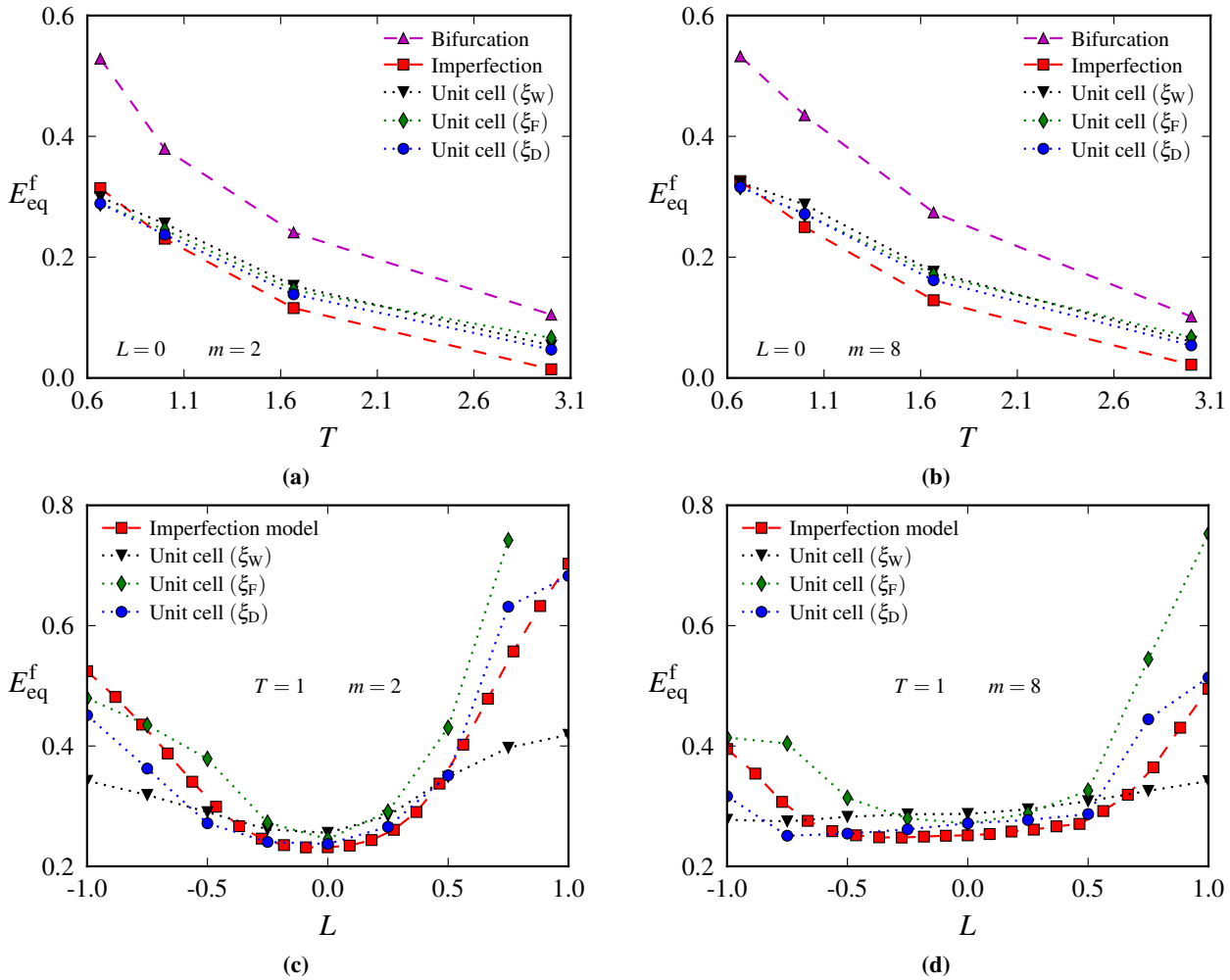

Figure 14: Comparison between failure strain determined from the unit cell simulations, the bifurcation analyses, and the imperfection band analyses. Results are shown for (a) $m = 2$ and (b) $m = 8$ in the case of generalized shear loading and various triaxiality ratios, and (c) $m = 2$ and (d) $m = 8$ for $T = 1$ and a number of Lode parameters.

the imperfection band model to further examine the influence of yield surface curvature on strain localization in the following.

6.5. Strain localization predictions using imperfection band analyses

Based on the notion that the imperfection band model gives a reasonable representation of the strain localization phenomenon for a spatially discretized band material, a large number of simulations were carried out using the two yield surface exponents $m = 2$ and $m = 8$ to study aspects of the matrix yield description on the failure strain. All calculations are performed with a material imperfection governed by the yield function in Equation (20) with an initial porosity of $f_0 = 0.005$ and with a sound material outside the band.

6.5.1. Effects of non-quadratic yield surface on failure strain

Figures 15a and 15b show the predicted failure loci for the quadratic and the non-quadratic yield surface in the case of stress triaxialities $T = 2/3$, 1, $5/3$, and 3 under a variety of Lode parameters. The effect of the Lode parameter is quite pronounced for the lower stress triaxialities, and the results show that the material is most susceptible to strain localization under loading conditions close to generalized shear regardless of the yield surface exponent. If the stress

triaxiality is increased, the non-uniformity of the velocity field is approaching the normal to the imperfection band, meaning that $\dot{\mathbf{q}}$ in Equation (47) becomes parallel to $\mathbf{n}$. This causes the deformations to localize in a dilatational mode for which stress states closer to generalized tension seem most critical, as seen from Figure 15b. This is actually in close agreement with the void growth rates from the unit cell results in Section 4.2, for which $L = -1$ resulted in the most rapid expansion of voids. We may infer from Figure 15b that the shift towards a dilatational band occurs earlier for $m = 8$, indicating that the Lode dependency of the matrix material facilitates such a transition. A puzzling effect is that the quadratic matrix yield surface is the most conservative in terms of failure strain for loading conditions approximately in the range $-1/2 \leq L \leq 1/2$. This range narrows down as the triaxiality decreases, however $m = 2$ still yields the lowest failure strain for stress states around $L = 0$, although the relative difference in this case is rather small.

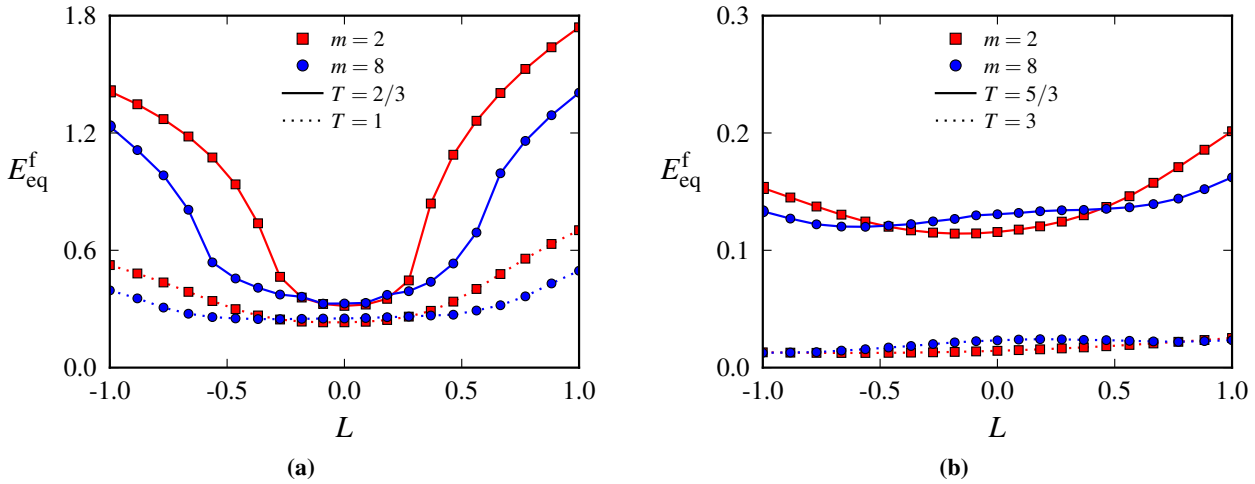

Figure 15: Failure strain levels pertaining to (a) $T = 2/3$ and 1, and (b) $T = 5/3$ and 3 for $m = 2$ and $m = 8$ against the Lode parameter.

As we also indicated in previous sections, differences for stress states around generalized shear might stem from the definition of the stress triaxiality. This was elucidated in terms of void growth rates in Section 4.2, although the effects of introducing a different triaxiality measure were not significant enough to yield conforming void growth for the two matrix descriptions. This gives an indication of the interplay between the intrinsic (matrix description) and extrinsic (void evolution) Lode effects. To assess the influence of the triaxiality definition, we have employed the redefined triaxiality ratio given by Equation (18) in a new set of strain localization calculations. Figures 16a and 16b show the results for (a) various stress triaxialities under generalized shear conditions, and (b) for various Lode parameters under constant stress triaxialities. By comparing results for T and T^* in these figures, we see that the use of a triaxiality ratio that is consistent with the equivalent stress measure gives similar failure strains for the quadratic and the non-quadratic matrix yield surface under stress states close to $L = 0$. However, marked differences prevail in the axisymmetric range of stress states, which follows directly from the fact that the two triaxiality definitions are identical for $L = \pm 1$. We should note that these results do not necessarily entail that it is recommended to use T^* rather than T, and we do not advocate using the former instead of the latter. However, they serve to demonstrate that this definition has an effect on the failure predictions.

From the results presented in Figures 15a and 15b we perceive that the non-quadratic matrix yield surface displays a flatter failure locus in terms of the Lode parameter than the quadratic matrix yield surface, at least for the stress triaxialities $T = 2/3$, 1, and $5/3$. The failure strain is lower for a larger set of Lode parameters and the Lode effect is correspondingly more prominent for the quadratic matrix yield surface than for the non-quadratic. Intuitively, the intrinsic Lode dependency would be expected to cause greater differences in the failure strain as the macroscopically applied deviatoric angle (or Lode parameter) changes because both the flow direction and the magnitude of the stress deviator are altered. However, these results suggest that the strain at localization is less influenced by the Lode parameter when the matrix yield surface is non-quadratic.

To shed some light on this matter, Figure 17 shows the stress state obtained inside the band as the material outside

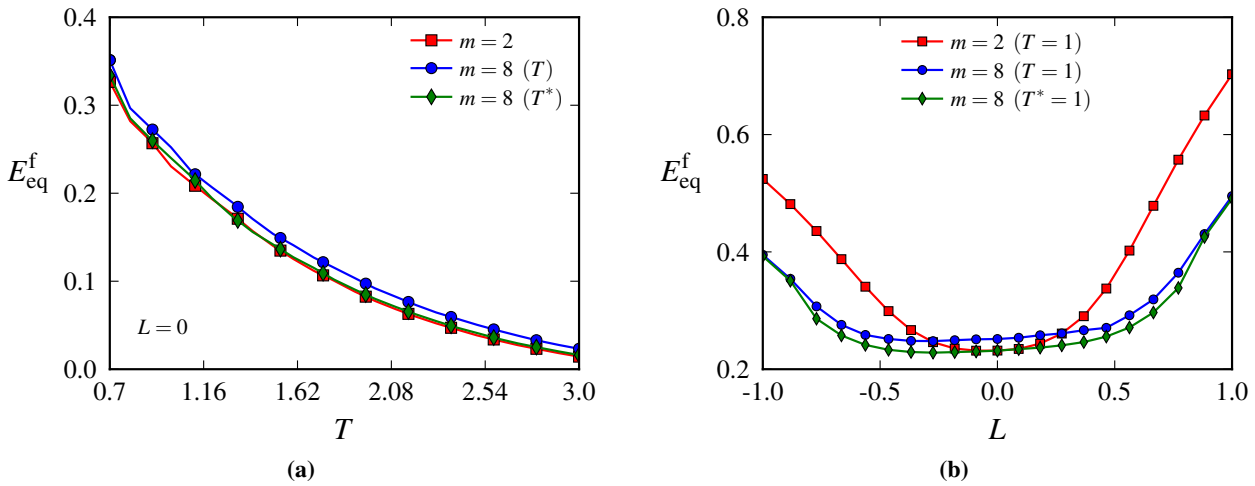

Figure 16: Comparison between failure strains for $m = 2$ and $m = 8$ using the two different triaxiality measures T and T^*. Figure (a) pertains to $L = 0$ and (b) for various Lode parameters at fixed triaxiality.

the band is proportionally stressed. Figures 17a and 17b show the change of the Lode parameter L_{b} inside the band as function of the accumulated plastic strain p_{o} of the bulk material in the case of macroscopic triaxialities $T = 2/3$ and $T = 1$, respectively. Figures 17c and 17d show similar results, but pertain to the stress triaxiality inside the band T_{b}. We readily infer from these data that the stress state inside the band deviates from the proportional state outside the band and becomes non-proportional due to the requirements of compatibility and equilibrium across the band interface. In terms of the Lode parameter, the stress state inside the band moves towards the most favourable state for localization, the one yielding least ductility, regardless of the externally imposed stress state. When the band encounters a stress state that satisfies $\det\left(\mathbf{n} \cdot \mathbf{C}^{\mathrm{t}}_{\mathrm{b}} \cdot \mathbf{n}\right) = 0$, the localization condition is met. As seen from the results in Figure 17, the critical state inside the band seems to be governed by a Lode parameter close to generalized shear $L_{\mathrm{b}} \approx 0$ for the given triaxiality levels. Since the non-quadratic matrix yield surface exhibits a high curvature close to the axisymmetric stress states (see Figure 2), it shifts more readily towards the favourable stress state for strain localization. The failure strain values are consequently reduced for $m = 8$ compared to $m = 2$, and the failure loci appear less Lode sensitive for the non-quadratic matrix yield surface. Moreover, we see from Figures 17c and 17d that the stress triaxiality is evolving quite differently depending upon the externally imposed stress state. An interesting effect is that the triaxiality inside the band is increasing for the generalized tension state ($L = -1$) while it decreases for generalized compression ($L = 1$). Since an increased hydrostatic stress inevitably accelerates void growth, this leads to reduced failure strain values for $L = -1$ compared to $L = 1$. This effect, in addition to that of the Lode parameter already mentioned, causes skew failure loci which are observed in this study (see Figures 14c, 14d and 15). This is in accordance with other studies (Barsoum and Faleskog, 2007b, 2011; Dunand and Mohr, 2014) using unit cell models. We emphasize that both the non-proportionality of the Lode parameter and of the stress triaxiality influence the macroscopic failure strain. Also, it should be remarked that a larger difference in failure strain between $L = \pm 1$ could have been obtained if the void growth from the porous plasticity model was in better correspondence to that obtained from the unit cell calculations in Section 4.2, since this would accelerate damage for generalized tension compared to generalized compression.

6.5.2. Influence of the porous plasticity parameters on the predicted failure strain

The q_i parameters determined from the calibration in Section 5.2, see Table 2, are different for the two yield surface exponents. Since these parameters influence the material response, we should elucidate their effects on the predicted failure strains and whether this alters the conclusions made in the previous section. To this end, we imposed the parameters of the original Gurson model ($q_1 = q_2 = q_3 = 1$) in the imperfection band analyses. In the following, we present only results for a triaxiality of $T = 1$.

As seen from Figure 18, the q_i parameters have only a moderate influence on the failure strain predictions. However, they seem to have a somewhat larger effect for the non-quadratic yield surface, although the difference is modest

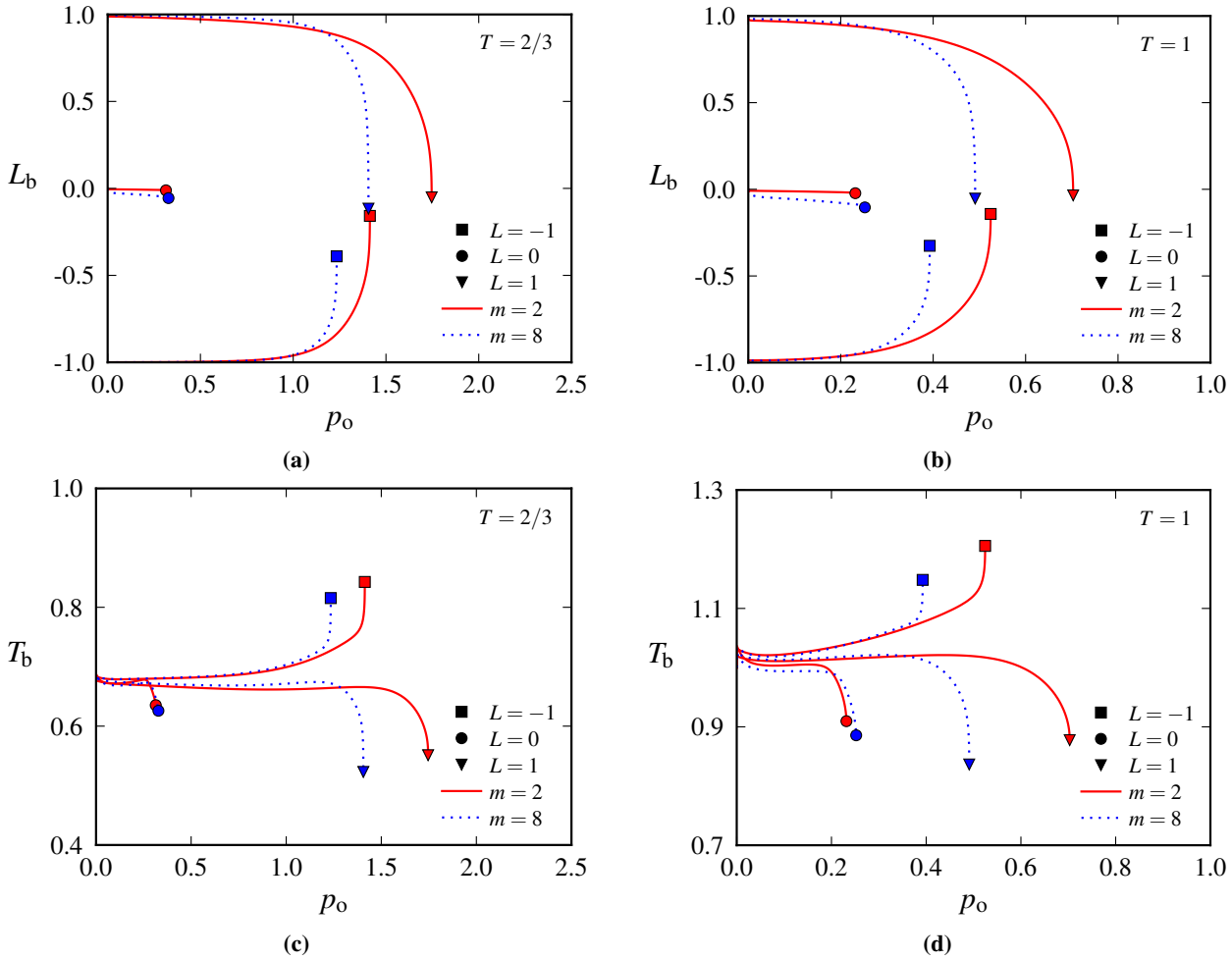

Figure 17: Variation of band quantities as function of the equivalent plastic strain outside the band p_o. The parameters L_b and T_b denote the Lode parameter and the stress triaxiality inside the band. Figures (a) and (b) pertain to the Lode parameter, while (c) and (d) show the stress triaxiality.

also for this matrix description. This might be related to the fact that the calibrated q_1 was slightly larger for $m = 8$ than for $m = 2$. The relative change is thus greater for the non-quadratic matrix yield surface which causes the deviation in the results. In agreement with the failure curves from the previous section, we find that the quadratic yield surface gives the lowest failure strain values around generalized shear whereas the non-quadratic is considerably more prone to localization as the magnitude of the Lode parameter is increased. Moreover, for all the loading cases shown, the calibrated model parameters yield the most conservative results in terms of failure strain. Hence, in addition to providing the best representation of the unit cell response in Section 4.2, these calibrated parameters are also favourable from an engineering perspective when estimating the failure loci. Note that this conclusion applies only to the original Gurson parameters and will certainly not hold for any given set of q_i parameters. In general, we have from Equation (22) that

$$\dot{f} = 3\dot{\Lambda}\,(1-f)\,f\frac{q_1 q_2}{\sigma_M}\sinh\left(\frac{3}{2}q_2\frac{\Sigma_h}{\sigma_M}\right) \tag{58}$$

The hyperbolic sine term will reduce the void growth rate when q_2 is lowered. But we infer that an increase of the product $q_1 q_2$ tends to accelerate the void growth. However, since $\dot{f}$ also depends upon the stress state, the situation is not as simple as determining whether the increase of $q_1 q_2$ outweighs the decrease due to $\sinh(q_2)$. A detailed explanation

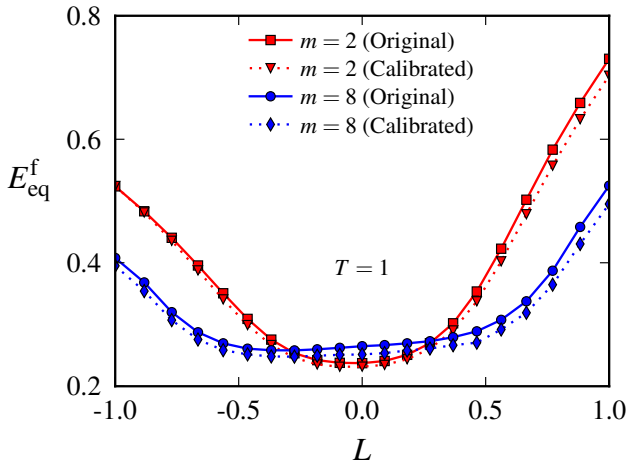

Figure 18: Failure loci for $m = 2$ and $m = 8$ using $T = 1$ and two different sets of q_i parameters. "Original" corresponds to $q_1 = q_2 = q_3 = 1$ and "Calibrated" to the parameters found from the calibration procedure.

for the difference obtained between the original and the calibrated set of q_i parameters in terms of the failure loci is rather involved and outside the scope of this paper. We believe that the difference can be broadly attributed to the changes in the stress path inside the imperfection band. However, the main message to be conveyed from the results displayed in Figure 18 is that the failure loci do not change much if the parameters $q_1 = q_2 = 1$ are used instead. Thus, the conclusions drawn from the results reported herein are deemed valid also for other sets of realistic q_i parameters.

7. Concluding remarks

A yield function incorporating effects of the third deviatoric stress invariant has been used to study the influence of a non-quadratic matrix yield surface on the overall yielding and strain localization in porous ductile solids. The results presented herein demonstrate that the intrinsic Lode dependency arising from a non-quadratic matrix yield surface has pronounced influence on the evolution of the approximative microstructure and the strain localization predictions.

Finite element simulations of an approximate material microstructure using a reduced unit cell model were conducted to examine the influence of a non-quadratic matrix yield surface on the resulting void evolution and macroscopic stress-strain response. The numerical results conclusively show that effects of the Lode parameter (or J_3) on the void growth and the mechanical response are persistent even when the matrix is Lode independent. When the matrix description is governed by the quadratic yield surface, the generalized tension states promote higher void growth rates, which were seen to successively decrease with increasing Lode parameter. The interplay between the Lode dependency of the matrix constitutive model and the Lode dependency resulting from the void evolution had pronounced influence on the response of the approximated RVE when a non-quadratic matrix yield surface was adopted. The generalized tension states still resulted in most rapid void growth, but the void growth rates were not monotonously decreasing with the Lode parameter for the non-quadratic yield surface. A redefined stress triaxiality ratio which incorporates the adopted equivalent stress measure was found to adjust the void growth to some extent for generalized shear states, but the effect was not sufficient to regain the monotonous decrease of the void growth rate with Lode parameter observed for the quadratic matrix yield surface.

A heuristic extension of the Gurson model in which the Hershey equivalent stress replaces the usual von Mises equivalent stress was proposed and calibrated from the unit cell results. The porous plasticity model was seen to account for the influence of the Lode parameter on the stress-strain and the porosity-strain curves. However, the Lode effects of the porous plasticity model were not sufficient to render the results similar to those from the unit cell calculations. Specifically, the porous plasticity model is not able to discern between states of generalized tension and generalized compression, which differ greatly in the unit cell calculations. In this regard, it is concluded that effects of void distortion must be included in the porous plasticity model, since the influence of the deviatoric stress state on the void shape evolution is also an apparent deficiency for a Lode-insensitive matrix formulation caused by the spherical

RVE used in the derivation of the Gurson model (Gurson, 1977). We note that such extensions of the Gurson model have already been made available in the literature using a different RVE (Gologanu et al., 1993; Madou and Leblond, 2012a,b) and by using a shear modification of the void growth equation (Nahshon and Hutchinson, 2008; Xue, 2008).

Strain localization analyses using the unit cell model revealed the prominent effects of a non-quadratic matrix yield function on the resulting failure strain. As a function of the Lode parameter, the failure strain exhibits a transition from the quadratic to the non-quadratic yield surface being more prone to strain localization. In the case of loading conditions close to generalized shear, we observed that the quadratic matrix yield surface led to earlier localization, whereas generalized tension states promote earlier strain localization for the non-quadratic yield surface. The difference in failure strain between the two yield surface exponents was much greater for the generalized tension state than for generalized shear loadings. Moreover, we showed that the prediction of strain localization using unit cell calculations is quite dependent upon the adopted localization indicator. This effect was more apparent for the generalized axisymmetric states, whereas in the case of generalized shear all three localization indicators employed herein predicted nearly the same failure strain.

Direct comparisons between the unit cell simulations, the bifurcation analyses, and the imperfection band analyses were made. Although the similarities between the different modelling strategies depended greatly upon the localization indicator used for the unit cell model, we found rather good agreement between the unit cell simulations and the imperfection band analyses on a qualitative basis. The bifurcation analyses, on the other hand, were found to overestimate the onset of strain localization. However, at high stress triaxiality levels, the strain localization predictions using the unit cell simulations were approaching the bifurcation analyses under generalized shear loading.

Strain localization analyses covering a wide range of stress states were undertaken by using imperfection band analyses. In the case of generalized shear states, the matrix with the quadratic yield surface is more susceptible to strain localization. However, we found that using a stress triaxiality ratio that incorporates the adopted equivalent stress measure gave conforming failure strain levels between the two yield surface exponents under generalized shear loading states on the entire stress triaxiality range $2/3 \leq T \leq 3$ investigated herein. As the deviatoric stress state approaches generalized tension or generalized compression, the non-quadratic matrix yield surface gave the lowest failure strain. Whether the material with the quadratic or the non-quadratic yield surface first undergo strain localization was found to depend upon the stress triaxiality. For the lowest stress triaxialities, the non-quadratic matrix yield surface led to earlier localization for nearly all the Lode parameters, whereas the opposite holds true for the highest stress triaxiality. The failure strain was shown to exhibit a minimum around generalized shear for the lower stress triaxiality ratios, while the minimum shifted somewhat towards $L = -1$ for increasing triaxiality values. Moreover, the failure strain was conclusively higher for generalized compression than for generalized tension, which causes non-symmetric failure loci. This effect was disclosed by considering the drift of the stress state inside the band towards a favourable state for localization, for which generalized tension states always reached the critical condition sooner than generalized compression states.

Acknowledgements

The financial support of this work from the Centre for Advanced Structural Analysis (CASA), Centre for Research-based Innovation (CRI), at the Norwegian University of Science and Technology (NTNU) and the Research Council of Norway through project no. 237885 (CASA) is gratefully acknowledged.

References

Abaqus, 2013. Version 6.13. Dassault Systèmes Simulia Corp., Providence, RI, USA.

Anand, L., Spitzig, W. A., 1980. Initiation of localized shear bands in plane strain. Journal of the Mechanics and Physics of Solids 28, 113–128.

Bao, Y., Wierzbicki, T., 2004. On fracture locus in the equivalent strain and stress triaxiality space. International Journal of Mechanical Sciences 46, 81–98.

Barsoum, I., Faleskog, J., 2007a. Rupture mechanisms in combined tension and shear-Experiments. International Journal of Solids and Structures 44, 1768–1786.

Barsoum, I., Faleskog, J., 2007b. Rupture mechanisms in combined tension and shear-Micromechanics. International Journal of Solids and Structures 44, 5481–5498.

Barsoum, I., Faleskog, J., 2011. Micromechanical analysis on the influence of the Lode parameter on void growth and coalescence. International Journal of Solids and Structures 48, 925–938.

Becker, R., Smelser, R. E., Richmond, O., Appleby, E. J., 1989. The effect of void shape on void growth and ductility in axisymmetric tension tests. Metallurgical Transactions A 20A, 853–861.
Belytschko, T., Liu, W. K., Moran, B., 2000. Nonlinear Finite Elements For Continua And Structures.
Benallal, A., 2017. Constitutive equations for porous solids with matrix behaviour dependent on the second and third stress invariants. International Journal of Impact Engineering, 1–16.
Benzerga, A. A., Leblond, J. B., Needleman, A., Tvergaard, V., 2016. Ductile Failure Modeling. International Journal of Fracture 201, 29–80.
Benzerga, A. A., Surovik, D., Keralavarma, S. M., 2012. On the path-dependence of the fracture locus in ductile materials - Analysis. International Journal of Plasticity 37, 157–170.
Besson, J., 2010. Continuum Models of Ductile Fracture: A Review. International Journal of Damage Mechanics 19, 3–52.
Bomarito, G., Warner, D., 2015. Micromechanical investigation of ductile failure in Al 5083-H116 via 3D unit cell modeling. Journal of the Mechanics and Physics of Solids 74, 97–110.
Bron, F., Besson, J., 2006. Simulation of the ductile tearing for two grades of 2024 aluminum alloy thin sheets. Engineering Fracture Mechanics 73, 1531–1552.
Budiansky, B., Hutchinson, J. W., Slutsky, S., 1982. Void growth and collapse in viscous solids. In: Mechanics of Solids: The Rodney Hill 60th Anniversary Volume. Pergamon Press, London, pp. 13–46.
Cazacu, O., Revil-Baudard, B., Chandola, N., Kondo, D., 2014. New analytical criterion for porous solids with Tresca matrix under axisymmetric loadings. International Journal of Solids and Structures 51, 861–874.
Cazacu, O., Stewart, J. B., 2009. Analytical plastic potential for porous aggregates with matrix exhibiting tension-compression asymmetry. Journal of the Mechanics and Physics of Solids 57, 325–341.
Clausing, D. P., 1970. Effect of plastic strain state on ductility and toughness. International Journal of Fracture Mechanics 6, 71–85.
Dæhli, L. E. B., Børvik, T., Hopperstad, O. S., 2016. Influence of loading path on ductile fracture of tensile specimens made from aluminium alloys. International Journal of Solids and Structures 88-89, 17–34.
Dæhli, L. E. B., Faleskog, J., Børvik, T., Hopperstad, O. S., 2017. Unit cell simulations and porous plasticity modelling for strongly anisotropic FCC metals. European Journal of Mechanics A/Solids 65, 360–383.
Doege, E., Seibert, D., 1995. Prediction of necking and wrinkling in sheet-metal forming. Journal of Materials Processing Technology 50, 197–206.
Dunand, M., Mohr, D., 2014. Effect of Lode parameter on plastic flow localization after proportional loading at low stress triaxialities. Journal of the Mechanics and Physics of Solids 66, 133–153.
Faleskog, J., Gao, X., Shih, C. F., 1998. Cell model for nonlinear fracture analysis – I. Micromechanics calibration. International Journal of Fracture 89, 355–373.
Gao, X., Zhang, G., Roe, C., 2010. A Study on the Effect of the Stress State on Ductile Fracture. International Journal of Damage Mechanics 19, 75–94.
Gologanu, M., Leblond, J. B., Devaux, J., 1993. Approximate models for ductile metals containing non-spherical voids – Case of axisymmetric prolate ellipsoidal cavities. Journal of the Mechanics and Physics of Solids 41, 1723–1754.
Gruben, G., Morin, D., Langseth, M., Hopperstad, O. S., 2017. Strain localization and ductile fracture in advanced high-strength steel sheets. European Journal of Mechanics - A/Solids 61, 315–329.
Gurson, A. L., 1977. Continuum Theory of Ductile Rupture by Void Nucelation and Growth: Part I – Yield Criteria and Flow Rules for Porous Ductile Media. Journal of Engineering Materials and Technology 99, 2—-15.
Haddag, B., Abed-Meraim, F., Balan, T., 2009. Strain localization analysis using a large deformation anisotropic elastic-plastic model coupled with damage. International Journal of Plasticity 25 (10), 1970–1996.
Haltom, S. S., Kyriakides, S., Ravi-Chandar, K., 2013. Ductile failure under combined shear and tension. International Journal of Solids and Structures 50, 1507–1522.
Hancock, J. W., Brown, D. K., 1983. On the Role of Strain and Stress State in Ductile Failure. Journal of the Mechanics and Physics of Solids 31, 1–24.
Hancock, J. W., Mackenzie, A. C., 1976. On the mechanisms of ductile failure in high-strength steels subjected to multi-axial stress-states. Journal of the Mechanics and Physics of Solids 24, 147–160.
Hershey, A. V., 1954. The plasticity of an isotropic aggregate of anisotropic face-centered cubic crystals. Journal of Applied Mechanics 21, 241–249.
Hill, R., 1963. Elastic properties of reinforced solids: Some theoretical principles. Journal of the Mechanics and Physics of Solids 11, 357–372.
Hill, R., 1967. The essential structure of constitutive laws for metal composites and polycrystals. Journal of the Mechanics and Physics of Solids 15, 79–95.
Hopperstad, O. S., Børvik, T., Langseth, M., Labibes, K., Albertini, C., 2003. On the influence of stress triaxiality and strain rate on the behaviour of a structural steel. Part I. Experiments. European Journal of Mechanics - A/Solids 22, 1–13.
Hosford, W. F., 1972. A Generalized Isotropic Yield Criterion. Journal of Applied Mechanics 39, 607–609.
Hosford, W. F., 1996. On the Crystallographic Basis of Yield Criteria. Textures and Microstructures 26, 479–493.
Kim, J., Gao, X., Srivatsan, T. S., 2004. Modeling of void growth in ductile solids: Effects of stress triaxiality and initial porosity. Engineering Fracture Mechanics 71, 379–400.
Koplik, J., Needleman, A., 1988. Void growth and coalescence in porous plastic solids. International Journal of Solids and Structures 24, 835–853.
Liu, Z. G., Wong, W. H., Guo, T. F., 2016. Void behaviors from low to high triaxialities: Transition from void collapse to void coalescence. International Journal of Plasticity 84, 183–202.
LS-OPT, 2017. LS-OPT Support Site.
URL `http://www.lsoptsupport.com/`
Madou, K., Leblond, J. B., 2012a. A Gurson-type criterion for porous ductile solids containing arbitrary ellipsoidal voids - I: Limit-analysis of some representative cell. Journal of the Mechanics and Physics of Solids 60, 1020–1036.
Madou, K., Leblond, J. B., 2012b. A Gurson-type criterion for porous ductile solids containing arbitrary ellipsoidal voids - II: Determination of yield criterion parameters. Journal of the Mechanics and Physics of Solids 60, 1037–1058.
Mandel, J., 1966. Contribution théorique à l'étude de l'écrouissage et des lois de l'écoulement plastique. Springer Berlin Heidelberg, Berlin,

Heidelberg, pp. 502–509.
McClintock, F. A., 1968. A Criterion for Ductile Fracture by the Growth of Holes. Journal of Applied Mechanics, 363 —- 371.
Mear, M. E., Hutchinson, J. W., 1985. Influence of yield surface curvature on flow localization in dilatant plasticity. Mechanics of Materials 4, 395–407.
Morgeneyer, T. F., Taillandier-Thomas, T., Buljac, A., Helfen, L., Hild, F., 2016. On strain and damage interactions during tearing: 3D in situ measurements and simulations for a ductile alloy (AA2139-T3). Journal of the Mechanics and Physics of Solids 96, 550–571.
Morgeneyer, T. F., Taillandier-Thomas, T., Helfen, L., Baumbach, T., Sinclair, I., Roux, S., Hild, F., 2014. In situ 3-D observation of early strain localization during failure of thin Al alloy (2198) sheet. Acta Materialia 69, 78–91.
Morin, D., Hopperstad, O., Benallal, A., 2017. On the description of ductile fracture in metals by the strain localization theory. Submitted for publication.
Nahshon, K., Hutchinson, J. W., 2008. Modification of the Gurson Model for shear failure. European Journal of Mechanics - A/Solids 27, 1–17.
Needleman, A., Rice, J., 1978. Limits to ductililty set by plastic flow localization. Mechanics of Sheet Metal Forming, 237 —- 265.
Needleman, A., Tvergaard, V., 1992. Analyses of Plastic Flow Localization in Metals. Applied Mechanics Reviews 45 (3), S3.
Needleman, A., Tvergaard, V., Hutchinson, J., 1992. Void Growth in Plastic Solids. In: Topics in Fracture and Fatigue. Springer New York, Ch. 4, pp. 145–178.
Papasidero, J., Doquet, V., Mohr, D., 2014. Determination of the Effect of Stress State on the Onset of Ductile Fracture Through Tension-Torsion Experiments. Experimental Mechanics 54, 137–151.
Papasidero, J., Doquet, V., Mohr, D., 2015. Ductile fracture of aluminum 2024-T351 under proportional and non-proportional multi-axial loading: BaoWierzbicki results revisited. International Journal of Solids and Structures 69-70, 459–474.
Perrin, G., Leblond, J. B., 1993. Rudnicki and Rice's Analysis of Strain Localization Revisited. Journal of Applied Mechanics 60, 842–846.
Rice, J. R., 1976. The Localization of Plastic Deformation. Proceedings of the 14th International Congress on Theoretical and Applied Mechanics 1, 207–220.
Rice, J. R., Tracey, D. M., 1969. On the ductile enlargement of voids in triaxial stress fields. Journal of the Mechanics and Physics of Solids 17 (3), 201–217.
Rudnicki, J. W., Rice, J. R., 1975. Conditions for the localization of deformation in pressure-sensitive dilatant materials. Journal of the Mechanics and Physics of Solids 23, 371–394.
Scales, M., Tardif, N., Kyriakides, S., 2016. Ductile failure of aluminum alloy tubes under combined torsion and tension. International Journal of Solids and Structures 97-98, 116–128.
Shinohara, Y., Madi, Y., Besson, J., 2016. Anisotropic ductile failure of a high-strength line pipe steel. International Journal of Fracture 197, 127 —- 145.
Soare, S. C., 2016. On the overall yielding of an isotropic porous material with a matrix obeying a non-quadratic criterion. International Journal of Engineering Science 104, 5–19.
Steglich, D., Wafai, H., Besson, J., 2010. Interaction between anisotropic plastic deformation and damage evolution in Al 2198 sheet metal. Engineering Fracture Mechanics 77, 3501–3518.
Tekoğlu, C., Hutchinson, J. W., Pardoen, T., 2015. On localization and void coalescence as a precursor to ductile fracture. Philosophical Transactions of the Royal Society of London A: Mathematical, Physical and Engineering Sciences 373, 1 – 19.
Thomas, N., Basu, S., Benzerga, A. A., 2016. On fracture loci of ductile materials under non-proportional loading. International Journal of Mechanical Sciences 117 (1), 135–151.
Tvergaard, V., 1981. Influence of voids on shear band instabilities under plane strain conditions. International Journal of Fracture 17, 389–407.
Tvergaard, V., 1982. On localization in ductile materials containing spherical voids. International Journal of Fracture 18, 237–252.
Tvergaard, V., 1987. Effect of yield surface curvature and void nucleation on plastic flow localization. Journal of the Mechanics and Physics of Solids 35, 43–60.
Tvergaard, V., 2012. Effect of stress-state and spacing on voids in a shear-field. International Journal of Solids and Structures 49 (22), 3047–3054.
Tvergaard, V., Van Der Giessen, E., 1991. Effect of plastic spin on localization predictions for a porous ductile material. Journal of the Mechanics and Physics of Solids 39, 763–781.
Vadillo, G., Fernández-Sáez, J., 2009. An analysis of Gurson model with parameters dependent on triaxiality based on unitary cells. European Journal of Mechanics - A/Solids 28, 417–427.
Westermann, I., Pedersen, K. O., Furu, T., Børvik, T., Hopperstad, O. S., 2014. Effects of particles and solutes on strength, work-hardening and ductile fracture of aluminium alloys. Mechanics of Materials 79, 58–72.
Wong, W. H., Guo, T. F., 2015. On the energetics of tensile and shear void coalescences. Journal of the Mechanics and Physics of Solids 82, 259–286.
Xue, L., 2008. Constitutive modeling of void shearing effect in ductile fracture of porous materials. Engineering Fracture Mechanics 75, 3343–3366.
Yamamoto, H., 1978. Conditions for shear localization in the ductile fracture of void-containing materials. International Journal of Fracture 14, 347–365.
Zhang, K., Bai, J. B., François, D., 2001. Numerical analysis of the influence of the Lode parameter on void growth. International Journal of Solids and Structures 38, 5847–5856.

Appendix A. Kinematic constraints to control stress path of unit cell model

The numerical procedure to impose nonlinear kinematic constraints which enable user control of the prescribed stress path will be reviewed herein. In the current exposition, the details for load control of a unit cell involving three normal deformation components and one shear component are presented, and the framework thus encompasses all relevant stress states for this study. Similar treatments have already been given by Barsoum and Faleskog (2007b, 2011), Dunand and Mohr (2014), and Wong and Guo (2015). We note that this method may be extended to include more degrees-of-freedom in order to study arbitrary band orientations, which is deemed important for anisotropic materials.

In the following, quantities $(\tilde{\circ})$ refer to the transformed basis related to the new set of degrees-of-freedom, while quantities $(\circ)$ are used in conjunction with the reference basis $\mathbf{e}_i$. To this end, we recast the macroscopic rate-of-deformation and the macroscopic stress tensors in vector form according to

$$\{\mathbf{D}\} = \begin{Bmatrix} D_{11} \\ D_{22} \\ D_{33} \\ 2D_{12} \end{Bmatrix}, \quad \{\boldsymbol{\Sigma}\} = \begin{Bmatrix} \Sigma_{11} \\ \Sigma_{22} \\ \Sigma_{33} \\ \Sigma_{12} \end{Bmatrix} \tag{A.1}$$

Under the assumption of homogeneous boundary conditions, the Hill-Mandel condition (Hill, 1963, 1967; Mandel, 1966) entails that the deformation power of the unit cell can be determined from the volume averaged Cauchy stress and rate-of-deformation, namely

$$\dot{W}_{\mathrm{d}} = V\boldsymbol{\Sigma} : \mathbf{D} = V\{\boldsymbol{\Sigma}\}^T\{\mathbf{D}\} = V\{\boldsymbol{\Sigma}\}^T[\mathbf{T}]\{\dot{\mathbf{U}}\} = \{\mathbf{P}\}^T\{\dot{\mathbf{U}}\} \tag{A.2}$$

where the relation between the displacement rates and the rate-of-deformation in Equation (31) has been invoked and a force vector on the form $\{\mathbf{P}\} = V[\mathbf{T}]^T\{\boldsymbol{\Sigma}\}$ has been introduced for convenience.

Let us further impose a linear transformation of the nodal displacement rates at the boundary $\dot{\mathbf{U}}$ according to

$$\{\dot{\tilde{\mathbf{U}}}\} = [\mathbf{A}]\{\dot{\mathbf{U}}\} \tag{A.3}$$

The equivalence of the work rate expressed in the two coordinate systems then yields

$$\dot{W}_{\mathrm{d}} = \{\mathbf{P}\}^T\{\dot{\mathbf{U}}\} = \{\tilde{\mathbf{P}}\}^T\{\dot{\tilde{\mathbf{U}}}\} \tag{A.4a}$$

$$\Rightarrow \quad \{\tilde{\mathbf{P}}\} = [\mathbf{A}]^{-T}\{\mathbf{P}\} = V[\mathbf{A}]^{-T}[\mathbf{T}]^T\{\boldsymbol{\Sigma}\} \tag{A.4b}$$

Specifically, we let the matrix product $[\mathbf{Q}] = [\mathbf{T}][\mathbf{A}]^{-1}$ define an orthogonal matrix, which then has the properties $[\mathbf{Q}]^T[\mathbf{Q}] = [\mathbf{1}]$ and $\det[\mathbf{Q}] = 1$. Accordingly, we may write

$$\{\tilde{\mathbf{P}}\} = V[\mathbf{Q}]^T\{\boldsymbol{\Sigma}\} \tag{A.5}$$

In order for a uniaxial loading state to prevail in the fictitious node, we choose a generalized force vector on the form

$$\{\tilde{\mathbf{P}}\} = \tilde{P}\{1 \;\; 0 \;\; 0 \;\; 0\}^T \tag{A.6}$$

in the transformed coordinate system. Now, let the transformation matrix $[\mathbf{Q}]$ be written in terms of the linearly independent column vectors $\{\mathbf{q}_i\}$, such that

$$[\mathbf{Q}] = [\mathbf{q}_1 \quad \mathbf{q}_2 \quad \mathbf{q}_3 \quad \mathbf{q}_4] \tag{A.7}$$

Since $[\mathbf{Q}]$ is orthogonal, we must have that $\{\mathbf{q}_i\}^T\{\mathbf{q}_i\} = 1$ and $\{\mathbf{q}_i\}^T\{\mathbf{q}_j\} = 0$ with $i \neq j$ and $i, j = 1, 2, 3, 4$. Note that there is no summation over indices in these relations. From Equation (A.5), we have that

$$V\{\boldsymbol{\Sigma}\} = [\mathbf{Q}]\{\tilde{\mathbf{P}}\} = \{\mathbf{q}_1\}\tilde{P} \tag{A.8}$$

The components of this expression read

$$V\Sigma_{11} = Q_{11}\tilde{P}, \quad V\Sigma_{22} = Q_{21}\tilde{P}, \quad V\Sigma_{33} = Q_{31}\tilde{P}, \quad V\Sigma_{12} = Q_{41}\tilde{P} \tag{A.9}$$

If we employ the stress ratios introduced in Equation (35), we find that

$$V\Sigma_{22} = V\rho_2\Sigma_{11} = \rho_2 Q_{11}\tilde{P} = Q_{21}\tilde{P} \tag{A.10a}$$
$$V\Sigma_{33} = V\rho_3\Sigma_{11} = \rho_3 Q_{11}\tilde{P} = Q_{31}\tilde{P} \tag{A.10b}$$
$$V\Sigma_{12} = V\rho_4\Sigma_{11} = \rho_4 Q_{11}\tilde{P} = Q_{41}\tilde{P} \tag{A.10c}$$

Thus, the relations between the four entries Q_{i1} from Equation (A.5) are given by

$$Q_{21} = \rho_2 Q_{11}, \quad Q_{31} = \rho_3 Q_{11}, \quad Q_{41} = \rho_4 Q_{11} \tag{A.11}$$

We then readily obtain

$$\{\mathbf{q}_1\}^T\{\mathbf{q}_1\} = Q_{11}^2\left(1 + \rho_2^2 + \rho_3^2 + \rho_4^2\right) = 1 \quad \Rightarrow \quad Q_{11} = \frac{1}{\sqrt{1 + \rho_2^2 + \rho_3^2 + \rho_4^2}} = \frac{1}{\rho_0} \tag{A.12}$$

and the first column is given by

$$\{\mathbf{q}_1\} = \frac{1}{\rho_0}\left\{1 \quad \rho_2 \quad \rho_3 \quad \rho_4\right\}^T \tag{A.13}$$

The remaining matrix components Q_{ij} are found from a Gram-Schmidt orthogonalization process where the mutually orthogonal unit vectors $\{\mathbf{q}_2\}$, $\{\mathbf{q}_3\}$, and $\{\mathbf{q}_4\}$ are calculated using $\{\mathbf{q}_1\}$ as the reference unit vector. We note that an explicit transformation matrix was proposed by Wong and Guo (2015).

With the transformation $[\mathbf{Q}]$ established, the nodal velocities at the unit cell boundaries are found by inverting Equation (A.3)

$$\{\dot{\mathbf{U}}\} = [\mathbf{A}]^{-1}\{\dot{\tilde{\mathbf{U}}}\} = [\mathbf{T}]^{-1}[\mathbf{Q}]\{\dot{\tilde{\mathbf{U}}}\} \tag{A.14}$$

This matrix equation provides nonlinear kinematic constraints which were implemented in the implicit finite element solver Abaqus/Standard using a Multi-Point Constraint (MPC) user subroutine. The constraint equations were solved by a mid-point algorithm in the numerical implementation and the resulting stress triaxiality and Lode parameter were checked to remain according to the prescribed values throughout the unit cell analyses. The boundary conditions prescribed to the fictitious node are then governed by

$$\tilde{U}_1 > 0 \quad \wedge \quad \tilde{P}_2 = \tilde{P}_3 = \tilde{P}_4 = 0 \tag{A.15}$$

where $\tilde{U}_1$ is the user-defined end displacement value of the fictitious node, and the transformed force components $\tilde{P}_{i\neq 1} = 0$ are used as constraints in the numerical procedure. The remaining nodal displacements in the fictitious node are in general non-zero, and must remain unspecified when the boundary conditions are prescribed to fulfil the nonlinear kinematic constraints.